Maija Rossi

# Magnetic Resonance Image Segmentation and Signal Analysis for Medical Applications

Maija Rossi

# Magnetic Resonance Image Segmentation and Signal Analysis for Medical Applications

Thesis for the degree of Doctor of Science in Technology to be presented with due permission for public examination and criticism in Sähkötalo Building, Auditorium S4, at Tampere University of Technology, on the 2nd of December 2011, at 12 noon.

**Supervisors**

Professor Hannu Eskola
Department of Biomedical Engineering, Tampere University of Technology
Tampere, Finland
Medical Imaging Centre, Pirkanmaa Hospital District
Tampere, Finland

Professor Seppo Soimakallio
Medical Imaging Centre, Pirkanmaa Hospital District
Tampere, Finland
School of Medicine, University of Tampere
Tampere, Finland

*To my granddad*

*2, 3, 5, 7, 11, 13, 17, 19, 23, 29, 31, 37, 41, 43, 47, 53*

**ABSTRACT**

Magnetic resonance imaging (MRI) is a medical imaging method used mainly for imaging soft tissue, such as the brain. It has various advantages, such as the noninvasive and nonionizing technique used; high contrast and signal-to-noise ratio; and excellent definition of both anatomical and physiological details.

Most of the current clinical MRI applications are qualitative. However, to reduce both intra- and interreader variability and thus, possibly, to improve patient diagnosis, treatment, and recovery, advantages may be gained through quantitative means. These include parametric imaging methods, such as $T_1$- and $T_2$-mapping, and analyses, such as histogram analysis, segmentation, and volumetry. These methods, along with qualitative imaging, were studied at various magnetic field strengths in healthy volunteers, non-Hodgkin lymphoma patients, patients with mild traumatic brain injury, and patients with symptoms of Parkinson's disease.

Quantitative volumetric analyses using semi-automatic segmentation of both MRI and computed tomographic images were easy and reliable but slow. In the lymphoma patients, the tumor volume was greatly reduced, beginning immediately after the initiation of chemotherapy. A small residual tumor volume six months after the completion of treatment was predictive of survival. Besides percentage volume changes, absolute tumor volumes and their absolute changes during early stages of treatment were considered useful. Several imaging sequences, including both quantitative and qualitative, were correlated with putative iron content. Their clinical correlation and the possibility as early biomarkers of disease progression require further investigation.

## ACKNOWLEDGEMENTS

discussions with me. Their interest towards my work was encouraging, and I learned much from them in a very short time. My supervisor Anca Oros, PhD, and other members of the MR group supported me not only in my work but also outside the research center. I also gratefully thank the professors in Finland, Prof. Kari Mäkelä and Prof. Jari Viik, for giving their time to correct my work.

I thank the pre-examiners of this thesis, Prof. Raj Rangayyan and Prof. Olli Gröhn, for their excellent commentary on the matter.

Surely, none of this would have been as pleasant if it was not nice to go to work in the morning. People at Komentokeskus have shared not only the room and the computers but also their lives with me. I thank Kirsi Holli, PhD, Lara Harrison, MD, PhD, Minna Sikiö, MSc, and other members of the Tissue Characterization Group for having made work fun!

Most importantly, I wish to thank my family. I sincerely thank my husband Jussi for loving me, supporting me, and enabling my work, down to the most basic parts of my life. I thank him for having prepared lunch for me to take to work, having fixed my bikes and waxed my skis for me to get to work, and having taken care of the children for me while I went to work, each and every day. I also thank him for our two children, and I thank the children, our daughter Aino and our son Väinö, for each smile I see on their faces and all of those hugs that make me warm inside.

Finally, I thank my granddad, Veikko Nevanlinna. I remember him teaching me the basics of mathematical thinking in a way a child could understand, even before I went to school. I remember vividly how he showed us the impossibility of proving that there is no life in outer space. His mere presence made me think scientifically. Therefore, I wish to dedicate this thesis to my 91-year-old granddad.

Tampere, November 2011

Maija Rossi

**CONTENTS**

## LIST OF ABBREVIATIONS AND SYMBOLS

| | |
|---|---|
| $\gamma$ | Gyromagnetic ratio |
| $\mu$ | Magnetic moment |
| $\tau$ | Time delay |
| $B_0$ | Main magnetic field |
| $S$ | Signal intensity |
| $T_1$ | Longitudinal relaxation time |
| $T_2$ | Transverse relaxation time |
| $T_2*$ | Effective transverse relaxation time |
| BOLD | Blood oxygenation level-dependent |
| CC | Corpus callosum |
| CPMG | Carr-Purcell-Meiboom-Gill |
| CSF | Cerebrospinal fluid |
| CT | Computed tomography |
| DTI | Diffusion tensor imaging |
| DWI | Diffusion-weighted imaging |
| EPI | Echo-planar imaging |
| fMRI | Functional magnetic resonance imaging |
| FDRI | Field-dependent relaxation rate increase |
| FLAIR | Fluid-attenuated inversion recovery |
| GM | Gray matter |
| GRE | Gradient echo |
| IR | Inversion recovery |
| MC | Multicontrast |
| MP-RAGE | Magnetization preparation rapid gradient echo |
| MR | Magnetic resonance |
| MRI | Magnetic resonance imaging |
| MRS | Magnetic resonance spectroscopy |
| MTBI | Mild traumatic brain injury |
| MTC | Magnetization transfer contrast |
| MTR | Magnetization transfer ratio |
| NHL | Non-Hodgkin lymphoma |
| NMR | Nuclear magnetic resonance |
| PET | Positron emission tomography |

| | |
|---|---|
| PD | Parkinson's disease |
| PD-W | Proton density-weighted |
| QUTE | Quantitative $T_2$* image |
| RF | Radio frequency |
| ROI | Region of interest |
| SAR | Specific absorption rate |
| SD | Standard deviation |
| SE | Spin echo |
| SNR | Signal-to-noise ratio |
| SPACE | Sampling perfection with application optimized contrasts using different flip-angle evolution |
| SWI | Susceptibility-weighted imaging |
| TAPIR | $T_1$ mapping with partial inversion recovery |
| TE | Echo time |
| TR | Pulse repetition time |
| TSE | Turbo spin echo |
| WM | White matter |

x

## LIST OF ORIGINAL PUBLICATIONS

I. **Rossi M**, Dastidar P, Pertovaara H, Kellokumpu-Lehtinen P-L, Järvenpää R, Luukkaala T, Rautakunnas S, Heinonen T, Soimakallio S, Eskola H. Response Analysis of Non-Hodgkin Lymphoma Using MRI-Based Volumes. *J Comput Assist Tomogr*. 2009;33:466-474.

II. **Rossi M**, Pertovaara H, Dastidar P, Järvenpää R, Luukkaala T, Rautakunnas S, Heinonen T, Eskola H, Soimakallio S, Kellokumpu-Lehtinen P-L. CT-Based Tumor Volume in Non-Hodgkin Lymphoma: Clinical Correlation and Comparison with MRI. *J Comput Assist Tomogr*. 2009;33:641-649.

III. Oros-Peusquens AM, **Laurila M**, Shah NJ. Magnetic field dependence of the distribution of NMR relaxation times in the living human brain. *MAGMA*. 2008;21:131-147.

IV. **Rossi M**, Dastidar P, Ryymin P, Ylinen A, Öhman J, Soimakallio S, Eskola H. Image quality and signal distribution in 1.5-T and 3-T MRI in mild traumatic brain injury patients. *Proc. SPIE* 7258, 72584M (2009); doi:10.1117/12.812224.

V. **Rossi M**, Ruottinen H, Elovaara I, Ryymin P, Soimakallio S, Eskola H, Dastidar P. Brain Iron Deposition and Sequence Characteristics in Parkinsonism: Comparison of SWI, $T_2$* Maps, $T_2$-weighted- and FLAIR-SPACE. *Invest Radiol*. 2010;45:795-802.

## 1. INTRODUCTION

Magnetic resonance imaging (MRI) is a rapidly developing noninvasive and nonionizing medical imaging method [Nakada 2007]. Most applications exploit nuclear magnetic resonance (NMR) signal coming form hydrogen nuclei in water molecules for their wide presence in the human body, but in principle, any nucleus with a spin quantum number different from zero is applicable. The NMR signal can be acquired after the excitation of the spin system as it returns to equilibrium. With the use of magnetic field gradients, the resulting signal can be localized and a MR image be formed.

In medicine, MRI is commonly used for imaging soft tissue, such as the brain, spine, or heart. MRI can be used to acquire both morphological and functional images. These images have a high value in the diagnostics and follow-up of several pathologies, such as cancer [Curvo-Semedo *et al*. 2011] and several neurological disorders [Symms *et al*. 2004, Mittal *et al*. 2009].

High magnetic fields with sufficient field homogeneity can be produced by means of superconductivity. The evident benefit of this possibility is an increased signal intensity, $S$, which allows for high spatial resolution and signal-to-noise ratio (SNR) and thus for the increased diagnostic value of MRI [Rooney *et al*. 2007].

Early devices used permanent magnets with field strengths far below one Tesla. Currently, clinical scanners provide field strengths of 1.5 or 3 Tesla, and research devices may reach 10 Tesla or higher [Moser 2010]. Modern devices may combine MRI with simultaneous positron emission tomography (PET) imaging [Catana *et al*. 2006].

New techniques and applications are needed for better patient diagnosis, treatment, and follow-up. In clinical environments, both MR imaging and image analysis are usually based on qualitative methods. These suit the intended purposes but may be affected by inter- and intraobserver variations. Reliable comparisons between patients thus suffer; therefore, at least for scientific purposes, quantitative image analysis should be performed such as parametric imaging, volumetry, and various methods of histogram analysis. Improving quantitative methods with respect to both their reliability and simplicity may well prove beneficial in not only research but also clinical use.

# INTRODUCTION

## 2.     AIM OF THE STUDY

Usually, quantitative methods are used in scientific studies, but in clinical routine, the primary choice is qualitative imaging. Therefore, investigating both methods is important. The aims of this study were

1. Testing and applying clinically applicable qualitative and quantitative MR imaging methods and analyzing the images with various segmentation techniques and signal parameters.

2. Comparing tissue relaxation times at different field strengths *in vivo*.

3. Showing that quantitative and semiquantitative image analysis methods for clinical MR images are efficient in the diagnostics and prognosis of malignant lymphomas and diseases of the central nervous system.

# AIM OF THE STUDY

## 3.     REVIEW OF THE LITERATURE

### 3.1.     MRI techniques

Nuclear magnetic resonance-based research may be considered to have initiated in the late 19th century, when Sir Joseph Larmor stated the relationship between the angular frequency of precession, $\omega$, and magnetic field strength, $B$, as $\omega = -\gamma B$, where $\gamma$ is the gyromagnetic ratio [Tubridy and McKinstry 2000]. In 1946, Felix Bloch and Edward Purcell measured magnetic resonance in solids and liquids [Bloch *et al.* 1946; Bloch 1946; Purcell *et al.* 1946]. In 1973, Paul Lauterbur introduced gradient fields for 2D image formation [Lauterbur 1973 and 1974]. In 1975, Richard Ernst first used the Fourier transform for image reconstruction [Kumar *et al.* 1975], and in 1977, Peter Mansfield proposed echo-planar imaging (EPI) [Mansfield 1977]. Around this time, the first medical images were presented, along with the first commercialized MRI scanners a few years later. Since then, several advanced imaging techniques have been introduced, such as diffusion-weighted and diffusion tensor imaging (DWI and DTI, respectively) [Filler *et al.* 1992], functional MRI (fMRI), which is based on blood oxygenation level-dependent (BOLD) contrast [Ogawa *et al.* 1993], and susceptibility-weighted imaging (SWI) [Haacke *et al.* 2004].

### 3.1.1.   Imaging principles

MRI techniques are based on the excitation and relaxation of spins, usually those of hydrogen in water molecules present in the human body. In the presence of a static main magnetic field, the spins are excited by the use of radio-frequency (RF) pulses which are often combined with gradient pulses. The RF pulses induce both the excitation of a spin system and phase coherence of the spins. After the RF pulse ends, the system rapidly recovers. The recovery to a lower energy level is presented by a longitudinal relaxation time, $T_1$, and the loss of phase coherence by a transverse relaxation time, $T_2$. These exponential decays are characterized by the Bloch equation

$$\frac{\mathrm{d}\boldsymbol{M}}{\mathrm{d}t} = \boldsymbol{M} \times \gamma \boldsymbol{B}_0 - \frac{(M_x \boldsymbol{i} + M_y \boldsymbol{j})}{T_2} - \frac{(M_z - M_0)\boldsymbol{k}}{T_1}, \tag{1}$$

where $\boldsymbol{M}$ is the net magnetization, $t$ is the time, $\gamma$ is the gyromagnetic ratio, $\boldsymbol{B_0}$ is the main magnetic field, and $\boldsymbol{i}$, $\boldsymbol{j}$, and $\boldsymbol{k}$ are the unit vectors in the $x$, $y$, and $z$ directions, respectively [Bloch *et al.* 1946; Bloch 1946]. The solution to this equation is

$$M_z(t) = M_0 + [M_z(0) - M_0] \cdot e^{-t/T_1} ,$$
$$M_{xy}(t) = M_{xy0} \cdot e^{-t/T_2}$$

(2)

where $M_0$ is the net magnetization at equilibrium. Due to static field inhomogeneities, the loss of phase coherence is more rapid than indicated by $T_2$. This decay is described by the effective transverse relaxation time $T_2^*$.

The spatial information of a MR signal is recorded using magnetic field gradients. These gradients can be used for slice selection and phase and frequency encoding. A receiver system records the amplitude, phase, and frequency of the MR signal. This frequency domain is called the *k*-space. Image formation is most commonly performed using the Fourier transform to turn the *k*-space information into a magnitude-reconstructed image [Kumar *et al.* 1975; Ljunggren 1983]. An alternative method is back projection, similar to that used in CT [Lauterbur 1973], where instead of the Fourier transform, the Radon transform is used to create the image [Hornak 1996]. Back projection can be accomplished using a $B_0$ sweep with a constant RF field (classical experiment) or an RF pulse sweep with a constant $B_0$ field (adiabatic experiment) [Tannús and Garwood 1997]. In all cases, spatial data are coded using the Larmor equation and field gradients.

### 3.1.2.  Effect of magnetic field strength

The relaxation process, especially in the case of $T_1$, is significantly affected by the main magnetic field. Indeed, several studies have shown that $T_1$ increases with the field strength whereas $T_2$ and $T_2^*$ decrease [Koenig and Schillinger 1969, Koenig *et al.* 1984, Johnson *et al.* 1985, Bryant 1996, Michaeli *et al.* 2002, Norris 2003, Mäkelä *et al.* 2004, Schenck and Zimmerman 2004, Bryant and Korb 2005, Ugurbil 2005, Chávez and Halle 2006, Halle 2006, de Graaf *et al.* 2006, Rooney *et al.* 2007, Pine *et al.* 2010, Pohmann *et al.* 2011]. Spin-lock investigations of $T_1$ in the rotating frame, $T_{1}\rho$, show relaxations similar to those of conventional $T_2$ methods [Markkola *et al.* 2001, Mäkelä *et al.* 2004, Gröhn *et al.* 2005], although their mechanisms are not fully understood [Mäkelä *et al.* 2004]. $T_2$ remains relatively constant up to fields of 1.5 T [Johnson *et al.* 1985], whereas $T_1$ strongly increases starting at very low fields, and the lengthening continues at high fields with decreasing field dependence [Rooney *et al.* 2007].

The $T_1$ relaxation time increases with the main magnetic field mainly because the energy difference between the "spin-up" and "spin-down" levels increases and is poorly transferred to the surroundings. The relaxation rate of pure water is constant with varying field strength, and the dispersion of $T_1$ in tissue is mainly attributed to molecular exchange between water and protein [Bryant 1996]. On the other hand, transverse relaxation times $T_2$ and $T_2^*$ are decreased at high fields in tissue. This is partly due to the increased dephasing caused by diffusion in local gradient fields, which in turn are caused by different magnetic susceptibilities in tissues [Mäkelä *et al.* 2004]. Another field-dependent $T_2$ relaxation mechanism is chemical exchange through which protons

switch from one pool to another—for example, from an –OH group to a –NH group. The chemical shift difference between the pools and the resulting dephasing rate are field dependent, enhancing relaxation at high fields. In the $T_2^*$ decay, static field inhomogeneities are not recovered, unlike that in $T_2$ measured by spin-echo techniques. The magnitude of these inhomogeneities grows with the main field, increasing the rate of dephasing. Thus, the field dependence of $T_2^*$ is greater than that of $T_2$.

High fields provide high SNR and spatial resolution; increased chemical shift for magnetic resonance spectroscopy (MRS); considerable benefits in BOLD, DWI, and DTI image quality; and increased $T_1$ for better background suppression in angiographic imaging [Duggan-Jahns 2008]. Although the increase in the main magnetic field is generally acknowledged to be advantageous, it also creates challenges with respect to image acquisition. First, due to changes in the relaxation times, pulse sequences have to be modified to maintain the desired image contrast. These modifications can be performed by altering parameters such as the echo time (*TE*), pulse repetition time (*TR*), and flip angle. Second, the specific absorption rate (SAR) is proportional to the square of the field strength, which is considered a significant safety issue and therefore limits the use of high-energy RF pulses. Third, at high fields, the center of the imaging volume experiences a higher RF field than the peripheral regions, leading to intensity modulations in the central position of an image. Despite these challenges, there is aspiration towards ever higher fields [Rooney *et al*. 2007].

### 3.1.3.  Pulse sequences

#### 3.1.3.1  Spin echo

Spin echo (SE) is one of the most conventional imaging sequences [Hahn 1950]. It excites the spin system with an RF pulse that tilts the net magnetization by an angle, e.g., 90°. After dephasing of the spins during *TE*/2, a spin refocusing pulse inverts the phase of the spins in the (x, y)-plane to recover the remaining phase coherence at a time *TE* measured from the initial RF pulse. The whole sequence is repeated after *TR*. SE is used in clinical practice to acquire $T_1$-weighted, $T_2$-weighted, and proton density-weighted (PD-W) images.

With the addition of an inversion pulse prior to the initial excitation pulse, image contrast can be modified. For example, with proper timing inversion recovery (IR) experiments can be used to suppress cerebrospinal fluid (CSF) and fat from the image, as in fluid-attenuated inversion recovery (FLAIR) or short $\tau$ inversion recovery (STIR) imaging, respectively.

#### 3.1.3.2  Gradient echo

Gradient echo (GRE) imaging does not recover the static field inhomogeneity-induced spin incoherence but creates an echo by inverting gradients. Gradient echo may be

performed by applying initially a negative gradient and then inverting it into a positive gradient in the readout direction. Gradient echo occurs when the gradient integral over time becomes zero. GRE imaging is fast and emits less energy to the tissue compared to SE because only one RF pulse is needed; furthermore, this pulse can be used at a very low energy, i.e., low flip angle.

An improvement in imaging speed can be accomplished using multislice imaging or EPI [Mansfield 1977], where switching frequency-encoding gradients and blipping phase-encoding gradients are used to acquire a total slice, or at least a large set of phase encoding lines, instead of one line after a single RF excitation. Traditional GRE images are $T_2^*$ weighted; however, the pulse design can be modified. For example, magnetization preparation rapid gradient echo (MP-RAGE) uses a preparative inversion pulse to introduce $T_1$ weighting to the image.

Susceptibility-weighted imaging (SWI) uses a filtered phase mask to multiply the original GRE magnitude images. The multiplication is performed several times to enhance the contrast in iron-containing structures, such as the veins and various structures in the basal ganglia region [Haacke *et al*. 2004, 2009a, 2009b, 2010b, Mittal *et al*. 2009, Robinson and Bhuta 2011].

### 3.1.3.3 Relaxation time mapping

In relaxation time mapping, several images with different weightings are used to create a parametric map.

In $T_1$ mapping, several images are acquired with the same $T_2$ weighting, i.e., with the same *TE*, but different $T_1$ weighting, i.e., with different *TI*. In a Look-Locker type acquisition, an inversion pulse is followed by several alpha pulses and the longitudinal magnetization approaches a value $M_\infty$ that is less than $M_0$ [Look and Locker 1970]. $T_1$ mapping with partial inversion recovery (TAPIR) is a Look-Locker-based method that begins with a nonselective saturation pulse to ensure that the value of $M_z$ at the time of each inversion pulse is always the same, independent of *TR*. The saturation pulse is followed by a time delay, $\tau$, and a nonselective inversion pulse. After spoiler gradients, the Look-Locker acquisition scheme follows. In TAPIR, the original Look-Locker method is improved by interleaving slices and adding an EPI-like acquisition [Steinhoff *et al*. 2001, Shah *et al*. 2001 and 2003, Zaitsev 2002, Zaitsev *et al*. 2003, Neeb *et al*. 2006]. The sequence is repeated once without the 180º pulse and once with an 180º – 180º combination pulse for RF inversion pulse inhomogeneity correction [Zaitsev *et al*. 2003]. The calculation of inversion efficiency based on these correction sequences is complex and is explained in detail in [Zaitsev *et al*. 2003]. The efficiency of the inversion pulse might decrease below 90% for a non-selective inversion pulse *in vivo* [Zaitsev *et al*. 2003]. The correction sequence can be performed with low spatial resolution for time saving.

$T_2$ mapping can be performed with a basic SE sequence with multiple 180º pulses [Carr and Purcell 1954]. The Carr-Purcell-Meiboom-Gill (CPMG) sequence accomplishes this with phase reversal between adjacent spin-refocusing pulses to minimize the effects of RF-field inhomogeneities [Carr and Purcell 1954; Meiboom and Gill 1958]. $T_2$ mapping can also be performed using the MapIt sequence which is commercially available [Hughes *et al*. 2007; Welsch *et al*. 2008 and 2010]. It uses a multiecho train, typically involving six echoes, and maps $T_2$ automatically pixel by pixel using a monoexponential, nonnegative least-squares fit [Hughes *et al*. 2007; Welsch *et al*. 2008 and 2010].

The quantitative $T_2$* image (QUTE) imaging scheme can be used for $T_2$* mapping. The sequence has similarities to the EPI sequence; however, the rapid reversal of the readout gradient is not accomplished for the whole *k*-space acquisition because the blipping phase gradient is lacking. Instead, several time points for the same *k*-space line are recorded after the slice-selective saturation pulse. After having acquired all the time points for a single line, the same line for all slices is measured, and the scheme is then individually repeated for each of the following lines [Dierkes *et al*. 2004; Neeb *et al*. 2006 and 2008]. The MapIt sequence can also be used to map $T_2$*, with a fitting procedure similar to that in $T_2$ mapping [Hughes *et al*. 2007; Welsch *et al*. 2008 and 2010].

### 3.1.4. Image contrast

Differentiation between tissues in an image can be presented with contrast. In this work, the peak-to-peak contrast, i.e., Michelson contrast,

$$c = \frac{S_a - S_b}{S_a + S_b},$$
(3)

is used, where $S_a$ and $S_b$ are the signal intensities of two adjacent structures a and b, respectively [Mischler 2011]. In most of the cases and sequences, contrast is primarily generated by differences in tissue properties, leading to changes in relaxation [Hornak 2006]. Contrast is also affected by the choice of pulse sequence and by modifications in the sequence design. Modifications in the pulse sequence design include changes in *TR*, *TE* and flip angle. The effects depend on the timing diagram. Short *TR* introduces $T_1$ weighting, whereas long *TE* introduces $T_2$ weighting in SE imaging, or $T_2$* weighting in GRE imaging. Decreasing the flip angle reduces $T_1$ weighting, which can be recovered by decreasing *TR*. Image contrast changes also between field strengths because of varying relaxation times. Field-dependent contrast changes have been used to create novel contrasts in both longitudinal [Ungersma *et al*. 2006] and transverse [Pfefferbaum *et al*. 2009] images.

## 3.2. Qualitative and quantitative MR imaging and analysis methods

The question whether an imaging method is quantitative or qualitative is rather philosophical [Sale *et al*. 2002]. Let us rely on saying that the "truth is what works" [Howe 1988] and proceed with the definition below. A large variety of MRI techniques have been proposed for different purposes. These include both qualitative and quantitative techniques. Similarly, there exist both qualitative and quantitative analysis methods (Table 1).

Qualitative MRI techniques result in one set of images (slices), whereas quantitative techniques produce two or more sets with different weightings. Qualitative MR image analysis is commonly performed by radiologists in diagnostics and refers to visual assessment. Quantitative analysis typically includes curve fitting between image sets acquired at different time points to extract a quantitative parameter, such as water content or relaxation time. However, the quantitative parameter to measure may also be as simple as the diameter or volume of a tumor, and such a quantitative parameter can be measured in both quantitative and qualitative images. In Table 1, contrast is considered to be the quantification of qualitative signal intensity and is therefore in between the quantitative and qualitative categories.

**Table 1**. Methods for qualitative and quantitative MR imaging and image analysis. Original publications of this thesis using each method are listed in Roman numbers.

| | Qualitative | | Quantitative |
|---|---|---|---|
| **Imaging** | $T_1$, $T_2$, $T_2$* weighting (I, II, IV, V) | | $T_1$, $T_2$, $T_2$* mapping (III, V) |
| | SWI (V) | | Phase mapping Susceptibility mapping |
| | PD-W | | $H_2O$ mapping |
| | MTC imaging | | MTR mapping |
| | DWI | | DTI |
| **Analysis** | | | $T_1$, $T_2$, $T_2$*, $H_2O$ fitting (III, V) |
| | | | Segmentation (I, II, III) |
| | Diagnostic evaluation | Contrast (IV, V) | |
| | Distribution of signal intensity | | Histogram analysis (III, IV) |
| | | | Volumetry (I,II) |

SWI = susceptibility-weighted imaging; PD-W = proton density-weighted; MTC = magnetization transfer contrast; MTR = magnetization transfer ratio; DWI = diffusion-weighted imaging; DTI = diffusion tensor imaging

### 3.2.1. Qualitative imaging, analysis, and applications

Qualitative imaging and image analysis are normally used in clinical environments. Qualitative imaging includes the most common imaging methods, e.g., PD-W, $T_1$-, $T_2$-, and $T_2$*-weighted imaging, FLAIR, and magnetization transfer contrast (MTC) imaging. Analysis is performed by visual assessment. Despite the availability of excellent radiologists, this may raise interindividual variations. The signal intensity may vary between patients and measurement sessions [Ebel *et al*. 2007; Franck *et al*. 2009]. The contrast between two tissues, however, is closer to being a quantitative measure because it depends on the percentage difference of the signal, not directly the signal intensity. Contrast may therefore be considered a semiquantitative measure.

### 3.2.2. Quantitative MR imaging

Quantitative MR imaging is mostly used for research purposes; however, there are also some commercially available quantitative imaging sequences for clinical use. Quantitative methods such as TAPIR [Steinhoff *et al*. 2001, Shah *et al*. 2001 and 2003, Zaitsev 2002, Zaitsev *et al*. 2003, Neeb *et al*. 2006], MapIt [Hughes *et al*. 2007, Welsch *et al*. 2008 and 2010], CPMG [Carr and Purcell 1954, Meiboom and Gill 1958], and QUTE [Dierkes *et al*. 2004, Neeb *et al*. 2006 and 2008] are based on multiple image sets acquired with different scanner parameters. Pixel-by-pixel curve fitting then results in a parametric map of a relaxation time, $H_2O$ content, magnetization transfer ratio (MTR), or other tissue-specific parameter. Ideally, after corrections for field inhomogeneities, parametric maps created by quantitative MRI methods are comparable worldwide, similar to CT images. However, due to both different hardware between manufacturers and the variety of different MRI sequences and fitting procedures variation in the results occurs between different groups around the world.

### 3.2.3. Quantitative MR image analysis methods

Quantitative image analysis of image sets acquired through quantitative MRI methods can be performed after pixel-by-pixel curve fitting. After defining a region of interest (ROI), various parameters can be measured. Thus, measurement of, e.g., the mean within the ROI, produces a quantitative number that allows for straightforward comparison with the bilateral hemisphere, another patient, or a healthy control group.

From another point of view, quantitative image analysis does not necessarily require quantitative MRI methods but some quantitative analyses can be performed with qualitative images. Image segmentation can be used for histogram analysis for mean, median, mode, standard deviation, range, kurtosis, or separability between two peaks, among others. One can analyze some of these independently, as in this work, or several combined, as in texture analysis [Lerski *et al*. 1993, Castellano *et al*. 2004, Holli *et al*. 2010, Sikiö *et al*. 2011]. In the case of parametric maps, straightforward analysis can be

performed, but qualitative images can also be analyzed. Preferably, normalization is required through a measure such as contrast.

Besides the measurement of histogram parameters, histogram analysis can be used for image segmentation and volume estimations. Image segmentation can be accomplished manually, semiautomatically, or in a fully automated manner. The manual outlining of structures is the most time-consuming method but may be necessary in cases of low contrast and SNR. Due to good image quality, most MR images are suitable for semiautomatic segmentation. Semiautomatic segmentation is based on manual outlines, histogram-based thresholding, and region growing [Heinonen *et al*. 1998a and b]. Semiautomatic segmentation is also time-consuming, if targeted to a large volume with high spatial resolution in the slice-encoding direction. There are a few methods proposed for fully automated segmentation of medical images, and they are applicable for limited purposes only [Atkins and Mackiewich 1998, Rangayyan *et al*. 2008 and 2009, Banik *et al*. 2008 and 2010, Dodin *et al*. 2010, Gao *et al*. 2010].

## 3.3.    Medical applications

MRI is widely used in clinical applications because of its noninvasive and nonionizing nature and excellent image contrast. $T_1$-weighted images are mainly used for morphological imaging, whereas $T_2$- and $T_2$*-based methods also reveal functional information. $T_2$- and $T_2$*-weighted images form the basis of several advanced imaging techniques, such as fMRI.

### 3.3.1.   Non-Hodgkin lymphoma

Non-Hodgkin lymphoma (NHL) is a group of malignant diseases. It is divided into four groups based on disease severity [Miller *et al*. 1981]. NHL may occur anywhere in the body. Therefore, besides disease severity, the symptoms depend on tumour location. One- and five-year survival ratios are 77% and 64%, respectively, and are predicted to rise [Finnish Cancer Registry 2009]. The disease is confirmed with both radiological examination and biopsy. Disease severity II-IV is usually treated primarily with chemotherapy, but consolidation radiotherapy is occasionally needed.

For optimal adaptation of treatment and thus improved prognosis, radiological monitoring of the clinical response to treatment is crucial. Both MRI and CT contribute to this aim. Additionally, PET may help in deciding upon the treatment plan by showing active tumor tissue [MacManus *et al*. 2007, Specht 2007, Lucignani 2007, Wu *et al*. 2011]. Although, often in clinical practice, resources are not available for very early response monitoring, treatment response should be evaluated as early as possible [Rodriguez 1998, Römer *et al*. 1998, Wu *et al*. 2011]. Treatment response is conventionally evaluated using one- or two-dimensional measurements of the lymphoma mass [Miller *et al*. 1981, Therasse *et al*. 2000 and 2006], whereby one-dimensionally, preference is given to the shorter axis perpendicular to the longest tumor

diameter [Therasse *et al*. 2006]. However, lymphomas are commonly irregular in shape; thus, full volumetric measurements are better suited for their evaluation than are one- and two-dimensional measures [Werner-Wasik *et al*. 2001; Prasad *et al*. 2002; Heussel *et al*. 2007].

NHL tumor volume can be calculated using either MRI or CT images. Because they are poorly suited for fully automatic segmentation, semiautomatic segmentation is optimal for their volumetric estimation [Mazzara *et al*. 2004]. In MRI, the images are sharper and have better SNR than in CT. Therefore, MR images are better suited for semiautomatic segmentation of the lymphoma mass than CT images. Furthermore, due to better contrast, they better differentiate tumors from the surrounding tissue and accurate localization of the lymphatic mass is easier.

### 3.3.2. Mild traumatic brain injury

In mild traumatic brain injury (MTBI), the brain is usually subjected to a blow. Despite the mild nature, the injury may be serious enough to affect memory, attention, mental organization, logical thinking, or processing speed [Erez *et al*. 2009]. For the treatment of MTBI, no bed rest is needed [de Kruijk *et al*. 2002], but the treatment of psychiatric and behavioral symptoms or physical rehabilitation may be needed [Cozzarelli 2010]. Patients usually recover fully, but some patients may have symptoms three months after injury [Erez *et al*. 2009, Fitzgerald and Grosson 2011]. The more serious condition, TBI, can be imaged and identified. However, 75%-90% of all clinical cases correspond to MTBI, a condition that is more difficult to image and diagnose than TBI [Erez *et al*. 2009, Haacke *et al*. 2010a, Fitzgerald and Grosson 2011].

MTBI is often difficult or impossible to detect with conventional MRI and this clinical condition lacks clear imaging standards [Fitzgerald and Grosson 2011]. After the initiation of this study, however, there has emerged a suggestion for an imaging protocol [Haacke *et al*. 2010a]. Besides conventional imaging, this protocol includes SWI [Haacke *et al*. 2004, 2009a, 2009b, 2010b, Mittal *et al*. 2009], DWI or DTI, and MRS.

In conventional MR imaging, lesions are observed in some but not all MTBI patients [Voller *et al*. 1999]. Lesions in the frontal regions of the brain predict poor outcome [van der Naalt *et al*. 1999]. Patients may suffer both global atrophy and GM atrophy [Cohen *et al*. 2007], and spectroscopy shows alterations in the levels of acetyl aspartate, choline, and creatine [Govind 2010]. In some patients, there may be changes in DTI, such as increased apparent diffusion coefficient [Goetz *et al*. 2004] or decreased fractional anisotropy [Niogi *et al*. 2008] in normal-appearing white matter. During cognitive tasks, fMRI may show decreased BOLD activity in the expected, predefined ROIs [Gosselin *et al*. 2011] but increased activity outside the expected ROIs [Zhang *et al*. 2010] in comparison to healthy controls. Changes in the texture of FLAIR and $T_1$-weighted images have also been detected [Holli *et al*. 2010]. Subtle changes in the texture, DTI, and fMRI may involve the mesencephalon and white matter tracts such as

corona radiata, corpus callosum (CC), uncinate fasciculus, centrum semiovale and internal capsule [Yuan *et al.* 2007, Niogi *et al.* 2008, Holli *et al.* 2010]. These findings encourage further investigations, even with conventional MRI sequences.

### 3.3.3. Parkinson's disease

Symptoms of Parkinsonism include several diseases among which Parkinson's disease (PD) is the most common diagnosis. The diagnosis is clinical, but final confirmation is not reached until post-mortem samples of the brain have been studied. PD is an incurable neurodegenerative disease, but its treatment improves the quality of life. Treatment may include medication, physical rehabilitation, and surgery. The symptoms include slowness in movement, muscular stiffness, resting tremor, and postural instability. The patients also have an increased risk of dementia. Motor impairment is derived from decreasing levels of dopamine which normally transfers information in the substantia nigra and is responsible for regulating voluntary movements and therefore the common symptoms of PD [Lees *et al.* 2009].

The synthesis of dopamine depends on iron levels [Berg 2007]. However, in its toxic form, iron is likely responsible for the PD-related neurodegeneration detected in the substantia nigra. In normal aging, iron deposits accumulate in the extrapyramidal nuclei of the brain [Hallgren and Sourander 1958, Pfefferbaum *et al.* 2009, Haacke *et al.* 2010b]. However, iron accumulation increases in several neurodegenerative diseases, such as PD. The exact location of iron accumulation in the brain varies between neurodegenerative diseases, and in PD primarily the substantia nigra is affected [Dexter *et al.* 1991, Antonini *et al.* 1993, Youdim and Riederer 1993, Ryvlin *et al.* 1995, Griffiths *et al.* 1999, Vymazal *et al.* 1999, Graham *et al.* 2000, Kosta *et al.* 2006, Martin *et al.* 2008, Brar *et al.* 2009, Zhang J *et al.* 2010]. Other reports regarding possible abnormal iron deposits in PD have indicated the caudate nuclei [Antonini *et al.* 1993], putamen [Drayer *et al.* 1986, Dexter *et al.* 1991, Chen *et al.* 1993, Antonini *et al.* 1993, Schwarz *et al.* 1996, Ryvlin *et al.* 1995, Graham *et al.* 2000, Kosta *et al.* 2006], and globus pallidus [Drayer *et al.* 1986, Dexter *et al.* 1991, Ryvlin *et al.* 1995, Griffiths *et al.* 1999].

Few changes due to PD can be observed in radiological examination, except for a decreasing volume in the substantia nigra [Graham *et al.* 2000; Menke *et al.* 2009]. However, with careful MRI examination, changes in iron deposits can be detected. Iron deposits can be indirectly measured using transverse-relaxation-based methods because they induce strong susceptibility gradients and thus enhance transverse relaxation. Suggestions for the use of MRI methods for iron quantification include $T_2$ and $T_2$* mapping, field-dependent relaxation rate increase (FDRI) [Pfefferbaum *et al.* 2009], and phase imaging, such as SWI [Haacke *et al.* 2004, 2009a, 2009b, 2010b, Mittal *et al.* 2009] and susceptibility mapping [Lotfipour *et al.* 2011].

## 4.     PATIENTS AND METHODS

### 4.1.     Patients and image acquisition

Each of the three patient studies was approved by the Ethics Committee of Tampere University Hospital, and all patients gave their written informed consent for the study. Imaging of the patients was performed at the Regional Medical Imaging Centre, Department of Diagnostic Radiology at the Tampere University Hospital, Finland. The healthy volunteers were imaged at the Institute for Medicine, Research Centre Jülich, Germany. Image acquisition was usually performed using a Siemens MRI device (Avanto, Trio, TrioTim, Siemens/Bruker MedSpec), and all the scanners run SYNGO software, though different version numbers. The lymphoma patients were imaged using a 1.5-T Signa HD Excite MRI system (GE Healthcare, Milwaukee, WI, USA); and with CT, using a Siemens Somatom Plus 4 system (Siemens, Erlangen, Germany). Table 2 presents the MRI methods used for each study.

**Table 2**. Sequences used in this thesis.

|  | Healthy volunteers | Non-Hodgkin lymphoma | Mild traumatic brain injury | Parkinsonism |
|---|---|---|---|---|
| $T_1$ mapping | X |  |  |  |
| $T_2$ mapping | X |  |  |  |
| $T_2$* mapping | X |  |  | X |
| $T_1$ weighting |  | X |  |  |
| $T_2$ weighting |  |  | X | X |
| $T_2$* weighting |  |  | X |  |
| FLAIR |  |  |  | X |
| SWI |  |  |  | X |
| CT |  | X |  |  |

FLAIR = Fluid-attenuated inversion recovery; SWI = susceptibility-weighted imaging; CT = computed tomography

The various methods and techniques used in this study are illustrated in Fig. 1. Throughout the text, the Roman numbers represent the original publications in this thesis.

### 4.1.1. Healthy subjects

Twelve healthy subjects were recruited for the study at the MR group, Institute for Medicine, Research Centre Jülich, Germany in 2007. The volunteer measurements were approved by the ethics committee. The sample featured eight males and four females, with ages ranging between 23 and 54 years (median 30.5 years). Imaging was performed at 1.5 T (Siemens Avanto, Erlangen, Germany), 3 T (Siemens Trio, Erlangen, Germany), and 4 T (Siemens/Bruker MedSpec, Erlangen, Germany) for each volunteer. An auto-align procedure was used to copy the coordinate system to obtain similar slice alignment between the scanners in a given volunteer. In each study, $T_1$, $T_2$ and $T_2*$ were measured using TAPIR, SE multicontrast (SE-MC), and QUTE, respectively [III]. First- and second-order shimming (zy, zx, xy, $z^2$, and $x^2$-$y^2$) was performed prior to imaging individually for each patient. The shimming included three linear channels and five
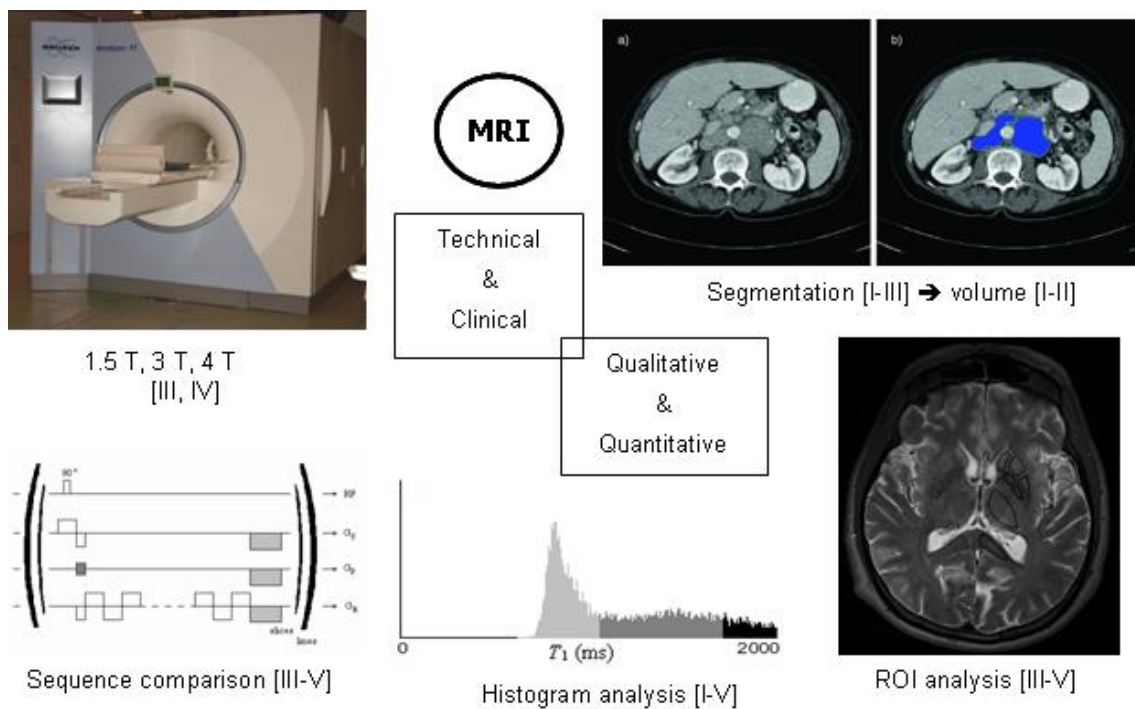


**Fig. 1.** Schematic representation of the various methods used for this study. The study included both technical aspects and clinical applications of image analysis of both qualitative and quantitative magnetic resonance imaging (MRI). Technical aspects included the effect of field strength and the use of various MRI sequences. The results were analyzed using histograms, segmentation, volumetry, and regions of interest (ROIs), including not only technical but also clinical questions. The Roman numbers (I-V) represent the original publications of this thesis.

nonlinear channels. The automated shimming procedure provided by the manufacturer was based on field mapping [Salem 2003].

### 4.1.2. Non-Hodgkin lymphoma patients

Thirty-four B-cell-type NHL patients were recruited at the Department of Oncology of the Tampere University Hospital during the period 2002-2006. The patients were imaged using a 1.5-T Signa HD Excite MRI system (GE Healthcare, Milwaukee, WI, USA) and an HD-CT Siemens Somatom Plus 4 CT system (Siemens, Erlangen, Germany) five times: at baseline (E1); one week after the initiation of chemotherapy (E2); after the fourth treatment course (E3); at the end of the treatment (E4); and at a six-month follow-up session (E5). Due to the minimum requirement of three completed scans, 29 patients were available for MRI analysis (median age 63 years, range 48 to 77 years; males:females = 19:10) and 25 for CT analysis (median age 63 years, range 34 to 77 years; males:females = 16:9). For volumetric analysis, $T_1$-weighted MRI images and CT images, both with contrast agents, were used. Besides volumetric analysis, the lymph nodes were measured one- and two-dimensionally. No exceptions to standard treatment were made. All patients underwent a thorough clinical examination [I, II].

### 4.1.3. Mild traumatic brain injury patients

Ninety-one MTBI patients were recruited at the Department of Neurology and Rehabilitation at the Tampere University Hospital. For the first group of 42 patients, MR imaging was performed at 1.5 T (Siemens Avanto, Erlangen, Germany) and for the remaining 49 patients at 3 T (Siemens TrioTim, Erlangen, Germany). To compare field strengths, 40 patients were randomly selected, 20 patients for each scanner. The median ages of the patients were 44 years (range 16 to 59 years) and 35 years (range 19 to 60 years) at 1.5 T and 3 T, respectively. The males:females ratios for the respective scanners were 8:12 and 11:9. Imaging was performed three weeks post-trauma. In this study, turbo SE (TSE) and GRE were used. The patients underwent a thorough clinical examination, including neurological and neuropsychological tests [IV].

### 4.1.4. Parkinson's disease patients

Fifty-two patients with symptoms of PD were recruited for the study at the Department of Neurology and Rehabilitation at the Tampere University Hospital. One patient withdrew, and scanning could not be completed. The median age of the remaining 25 male and 26 female subjects was 69 years (range 40 to 86 years). All patients were imaged on a 3-T MRI scanner (Siemens TrioTim, Erlangen, Germany). For this study, the following sequences were acquired: SWI, $T_2$* mapping using the MapIt sequence, $T_2$-weighted SE, and FLAIR. The last two sequences were acquired using the sampling perfection with application-optimized contrasts using different flip-angle evolution (SPACE) sequence [Lichy *et al*. 2005]. The patients underwent a thorough clinical

examination, including neurological and neuropsychological tests [V]. First- and second-order tune-up shimming was performed prior to imaging.

## 4.2.    Image analysis

Volumetric analysis was performed using the semiautomatic segmentation software Anatomatic$^{TM}$ 2.23 [Heinonen *et al.* 1998a] [I, II]. The Anatomatic$^{TM}$ software has been developed at the Department of Biomedical Engineering in Tampere University of Technology, Finland. Relaxation time mapping was performed pixel by pixel using the in-house QI software [Neeb *et al.* 2006] [III] or the commercial software provided by Siemens [V]. Other image analysis was performed applying the software ImageJ 1.40g (National Institutes of Health, USA). Statistical analysis was performed using SPSS 17 (SPSS Inc., Chicago, Illinois, USA) [I, II, V] and curve fitting using Origin software (Origin 7.0 SR0, v7.0220, OriginLab Corporation, Northampton, MA, USA) [III, IV].

### 4.2.1.    Segmentation

Image segmentation was performed manually, semiautomatically, and automatically. Semiautomatic segmentation, using the Anatomatic$^{TM}$ software, was used to delineate the lymphomas in MR images [I] and some CT images [II], though manual segmentation was needed during CT image analysis most of the times [II]. Semiautomatic segmentation was based on a combination of thresholding and manual outlining of objects followed by the application of region growing technique (Fig. 2). In manual segmentation, only manual outlining was used prior to region growing. An experienced radiologist supervised the selection of lymphatic tissue [I, II]. In the Anatomatic$^{TM}$ software, the user was not able to see the $T_1$ histograms that were the base of windowing and thresholding.

In the case of the healthy volunteers, segmentation of white matter (WM) and gray matter (GM) in the brain was performed using the $T_1$ maps and the ImageJ software. First, manual segmentation was used to remove the skull and fatty layers. Second, the threshold levels for WM and GM were determined. The decision was based on the $T_1$ histograms averaged over all volunteers, prior knowledge of the $T_1$ values in known WM and GM, and visual assessment of the images. Third, the WM and GM were segmented using automatic thresholding [III]. The clarifying histograms and segmented images will be presented in the results section. In the ImageJ software the user was able to see the $T_1$ histograms that were the base of windowing and thresholding.
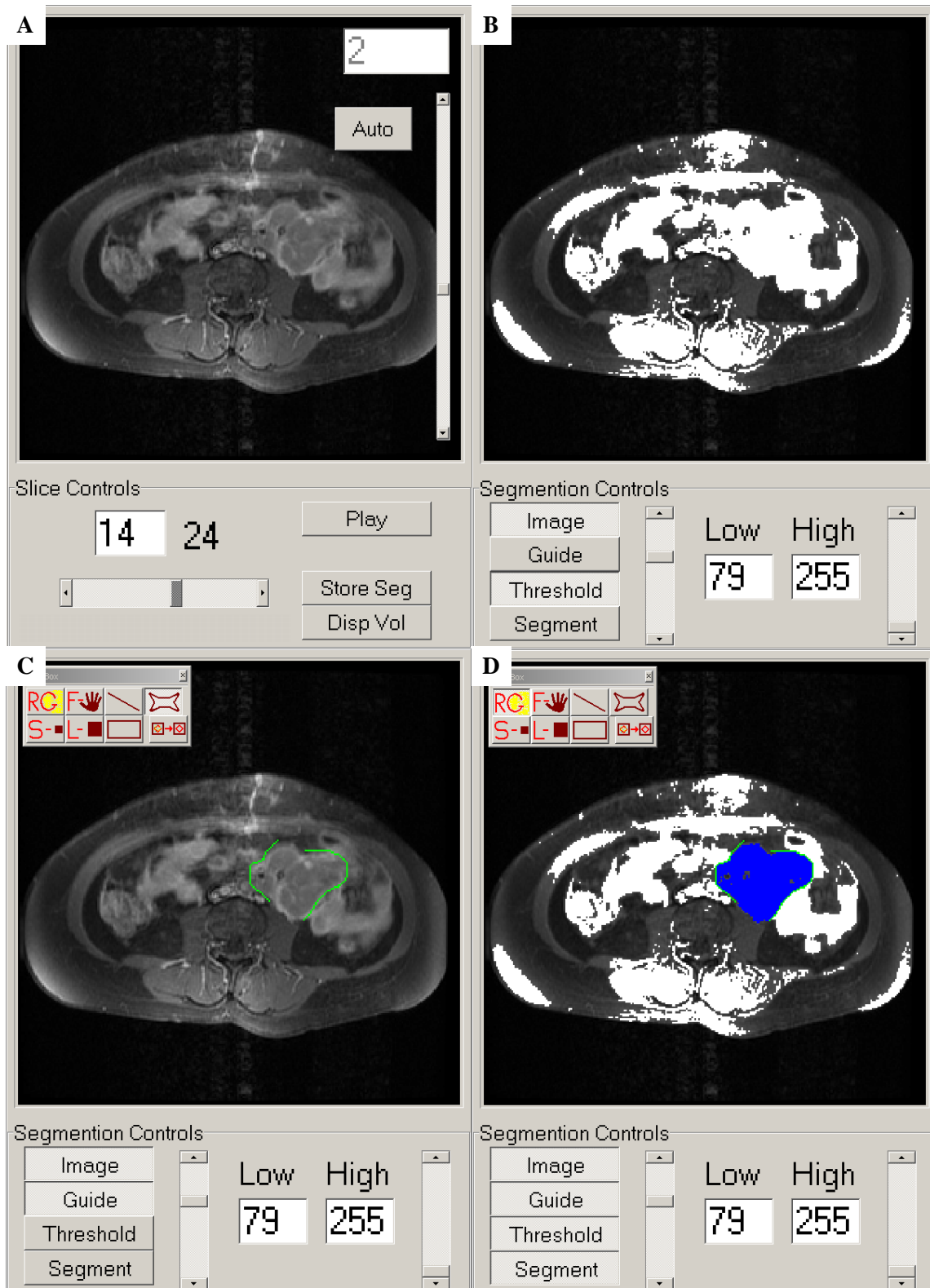
**Fig. 2.** Segmentation of an abdominal MR image of a non-Hodgkin lymphoma patient with the Anatomatic[TM] software. The procedure includes adjusting contrast (A), setting threshold levels (B), manually outlining the object where necessary (C), and selecting the lymphatic tissue using region growing (D).The tumor is seen as a hypodense multilobular soft tissue mass with the presence of peripheral contrast enhancement, compressing the surrounding bowels.

### 4.2.2. Signal analysis

Signal analysis was performed on various ROIs, selected using manual ROI selection [III-V], or fully automatic segmentation [III]. The MR signal was analyzed using the gray-level histograms of the ROIs [III-V]. The analysis included determination of the peak position (the average or median of signal intensity or a quantitative parameter, such as the relaxation times) and peak width (or standard deviation, SD). In most cases these parameters are automatically computed by the software, although they are implicitly based on histograms. However, in publications III and IV, the histograms were plotted for the ROIs. Several fits were calculated based on Gaussian distribution [III, IV]. These were used to visualize the ability of MRI to separate between various biological tissues.

In publications III and V, the time series of signal decay was fitted pixel by pixel with exponential models based on Equation 2. In healthy volunteers, the user was required to manually provide the software, developed in-house, with some sequence parameters and the MR images [III]. In patients with symptoms of PD, the commercial software automatically calculated the relaxation times [V].

### 4.2.3. Statistical analysis

Comparisons between two groups were usually performed using Student's t-test. However, in cases in which the Kolmogorov-Smirnov test revealed non-Gaussian distribution, the Wilcoxon signed ranks test or Mann-Whitney U-test was used to compare paired and unrelated samples, respectively. Comparisons between several groups were performed with the median test due to significantly skewed distributions in the NHL study. Correlations were tested using Pearson's correlation; or Spearman's rho correlation in the case of nonparametric data or a significantly skewed distribution.

## 5.    RESULTS

## 5.1.    Segmentation

In this study, the applications required three types of segmentation methods: manual, semiautomatic and fully automatic segmentation.

### 5.1.1.  Techniques

Semiautomatic segmentation of lymphomas was time-consuming, taking 1.5 to 2.5 hours per patient to analyze three to five datasets [I, II]. The time required depended on the tumor size and location. The location of the tumor affected the grade indicating how much semi-automatic segmentation could be used, i.e., how much manual interference was required to accurately delineate the lymphoma mass from the surrounding tissue. In CT, due to lower contrast and SNR compared to MRI, semiautomatic segmentation could not be effectively used and required replacement by manual segmentation. Intra- and interobserver variation was less than 10%, with larger percentage variations in small-sized lymphomas than in large-sized lymphomas.

The two imaging modalities were well intercorrelated with slightly larger volumes in MRI than CT [II]. Volumetric measurements also correlated well with one- and two-dimensional tumor measurements in both MRI and CT, although slight deviation was observed [I, II].
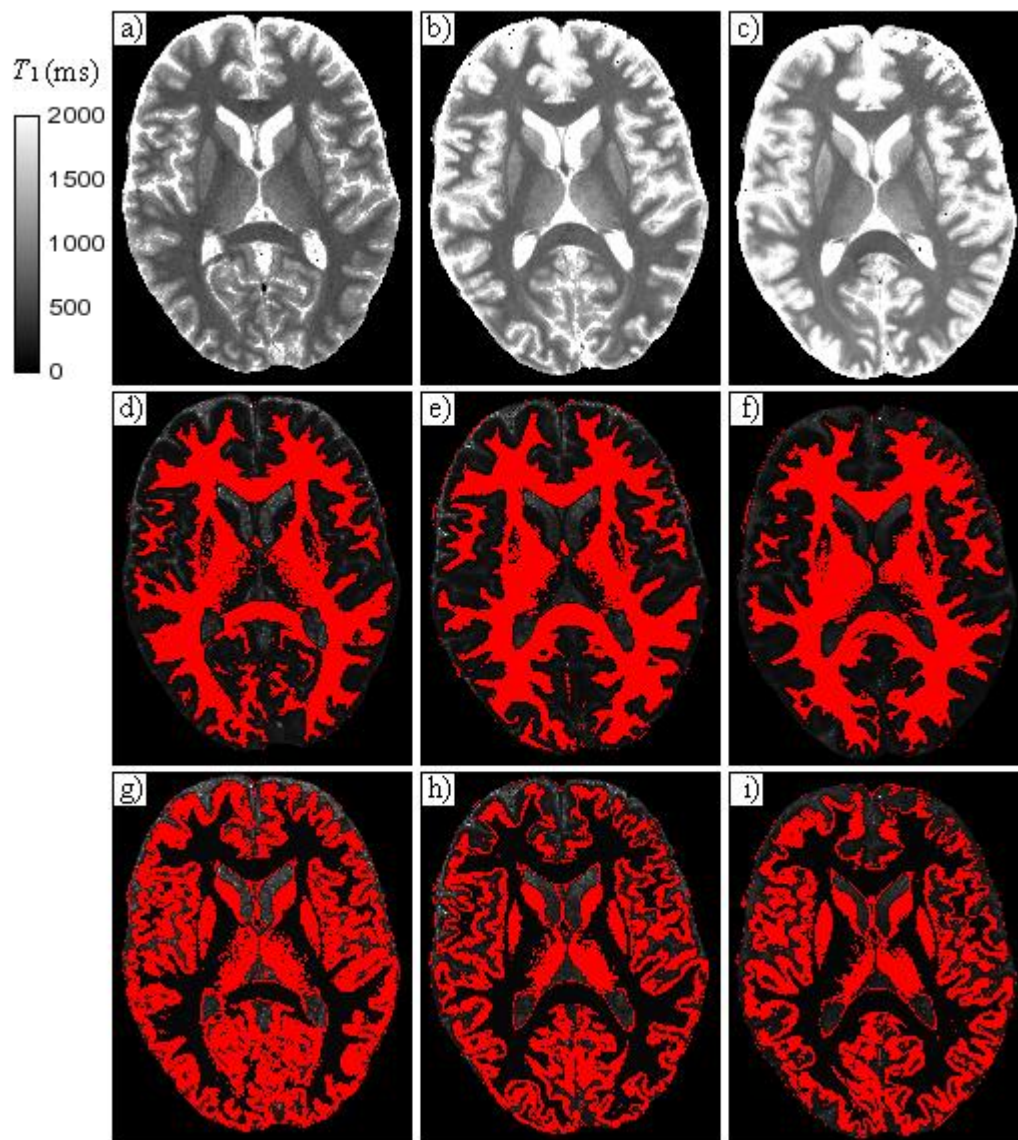
**Fig. 3.** One slice of the quantitative $T_1$ map of one volunteer using the field strengths 1.5 T (a), 3 T (b), and 4 T (c) with the calibration bar at the left. The skull has been segmented out manually. In (d)-(f) the same slice is shown after the segmentation of the white matter, and in (g)-(i) after the segmentation of the grey matter [Laurila 2007].

**Table 3.** Segmentation limits (ms) for white and gray matter at 1.5 T, 3 T and 4 T in publication III [Laurila 2007].

|               | 1.5 T     | 3 T      | 4 T       |
|---------------|-----------|----------|-----------|
| White matter  | 430…780   | 550…950  | 600…1050  |
| Gray matter   | 781…1400  | 951…1550 | 1051…1600 |

Fully automatic segmentation of WM and GM in healthy subjects [III] was rapid and could be performed using parametric $T_1$ maps (Fig. 3). However, preparation was needed to decide the $T_1$ limit for WM and GM. This preparation included prior knowledge of $T_1$ at each field strength from both previous literature and the volunteers imaged with the same sequence and on the same scanners, knowledge of the anatomical distribution of WM and GM in the brain, and histogram analysis on $T_1$ distribution in known WM and GM.

Using the appropriate limits selected for the particular scanners and sequences used in publication III (Table 3), the brain was segmented automatically. Selection of the limits is described in section 5.2.3. After segmentation, visual inspection confirmed the success in every image separately, one of which is shown in Fig. 3. The lengthening of $T_1$ values can be observed at the top row as brightening from left to right, as the calibration is set equal at each field. The segmentation results are nearly identical, considering the slightly different slice positioning, especially at 4 T where the auto-align showed poor performance.

## 5.1.2. Clinical correlation

After the segmentation and volumetric calculation of the target tumors, rapid volume decrease was observed in NHL patients immediately after the first chemotherapy cycle in both MRI and CT images [I, II]. The initial tumor volume was slightly larger in patients with previously untreated lymphoma than in patients with a relapse [I, II]. In CT, larger tumor volumes at E4 predicted higher mortality than smaller residual volumes (Fig. 4 b). In MRI, the tumor volume decrease during the first week of chemotherapy was larger in patients with higher mortality than in patients with lower mortality, but the difference was not statistically significant (Fig. 4 a) [I]. Similar results were not obtained with the CT data that had a slightly smaller patient population [II]. This result was not supported by our one- and two-dimensional measures of the same patient population.
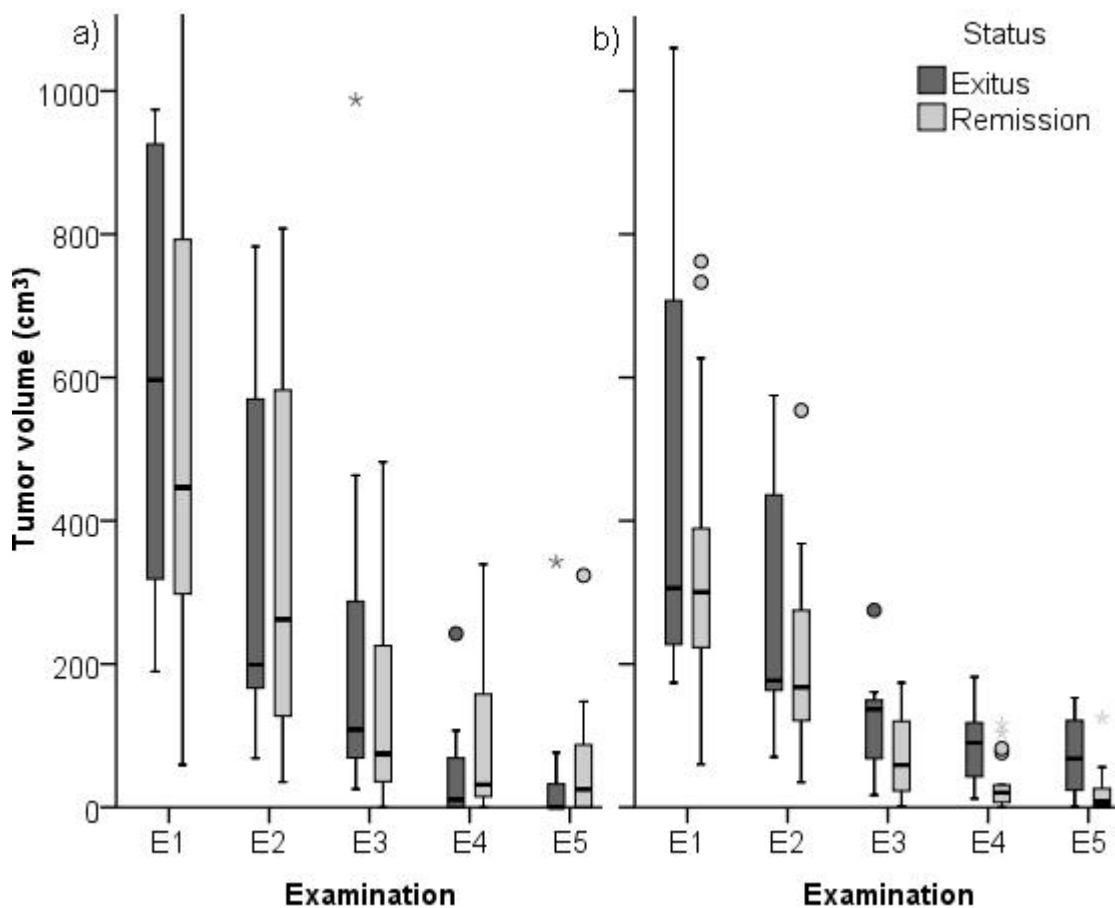


**Fig. 4.** Tumor volumes of the deceased and survived patients at the five examination time points in MRI (a) and CT (b) images. Medians (lines), interquartile range (boxes), 95% confidence intervals (T-bars) and outliers (spheres and stars).

## 5.2. Signal analysis

Signal analysis included curve fitting of the parametric relaxation times $T_1$, $T_2$ and $T_2$*
[III, V], histogram analysis [III, IV], and contrast measurements [IV, V].

### 5.2.1. Relaxation times

 In the healthy human brain, a significant increase in $T_1$ and decrease in $T_2$ and $T_2$* with
main magnetic field strength was observed [III]. The average $T_1$ at each field for the
segmented WM and GM is presented in Fig. 5. The $T_1$ values increased significantly
with the increasing main magnetic field in both WM and GM. The dispersion of $T_2$ and
$T_2$* is shown in Fig. 6. Both $T_2$ and $T_2$* decreased with the increasing main magnetic
field. The decrease in $T_2$* was significant in all ROIs, whereas that in $T_2$ was modest and
inconsistent in the red nucleus, thalamus, and caudate nucleus.
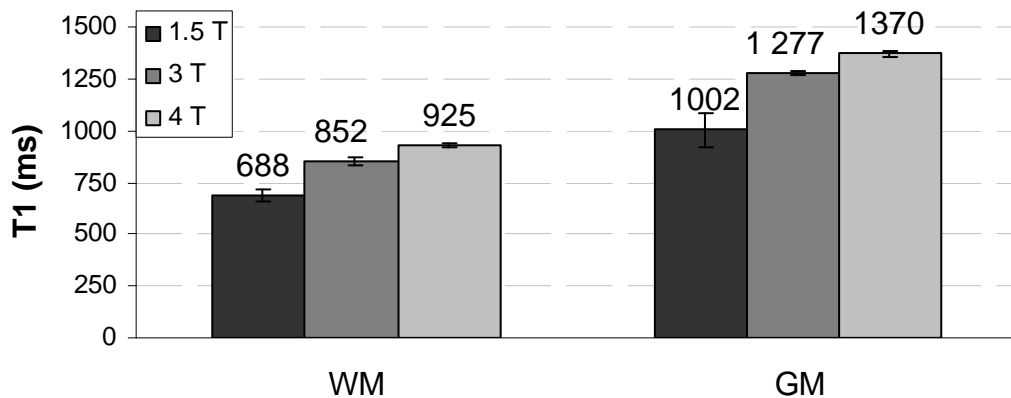


**Fig. 5.** Average white matter (WM) and grey matter (GM) $T_1$ in the 12 healthy
volunteers. Modified from [Laurila 2007].
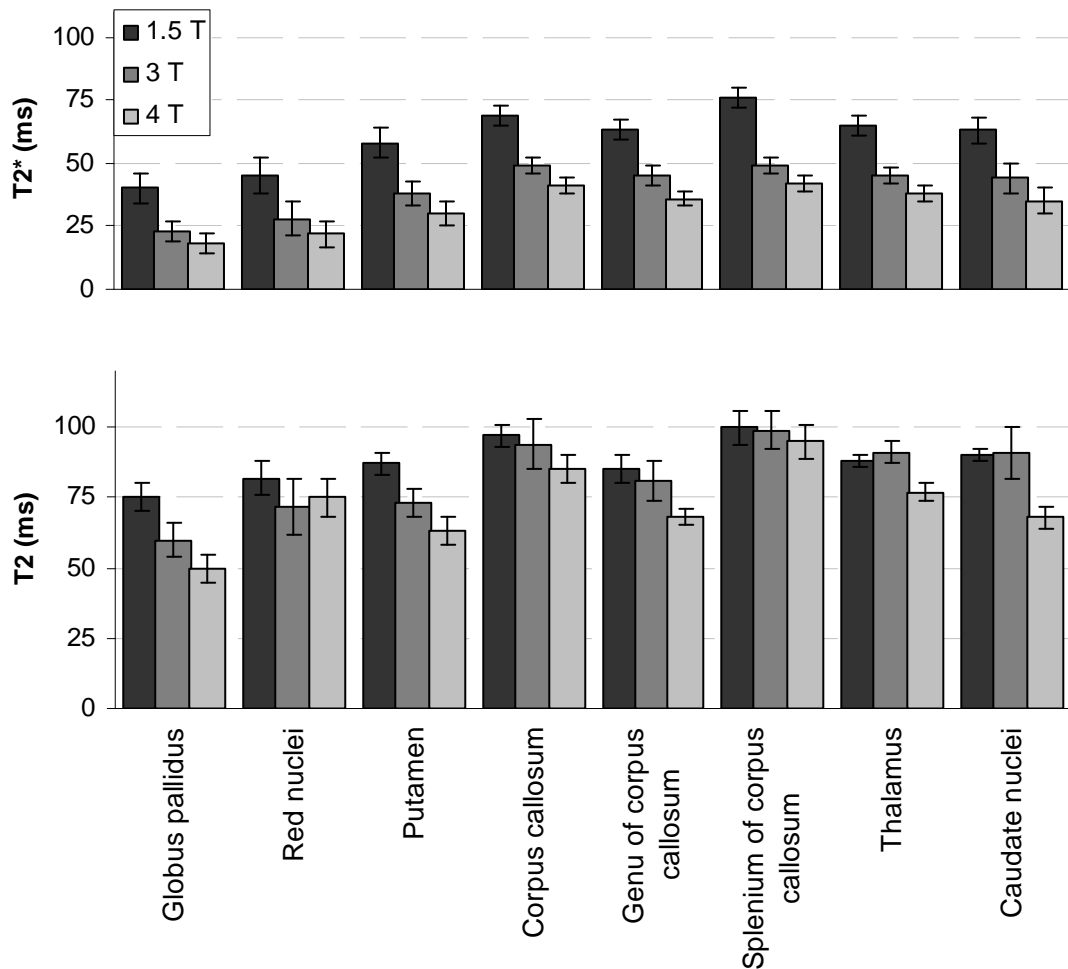
**Fig. 6.** Average $T_2$ and $T_2$* in the 12 healthy volunteers. Modified from [Laurila 2007].

The $T_2$* relaxation times at 3 T in patients suspected of having PD [V] are shown in Fig. 7. The difference between healthy and diseased brain, imaged with QUTE and MapIt, respectively, is expressed as a percentage. Except for the genu of CC, the $T_2$* relaxation was considerably faster in the healthy subjects measured with the QUTE sequence than in the patients showing clinical symptoms of Parkinsonism, measured with the MapIt sequence. Relaxation time maps at the three fields are shown in Fig. 8 with similar scaling within a given relaxation time for each of the three field strengths in a healthy volunteer [III].
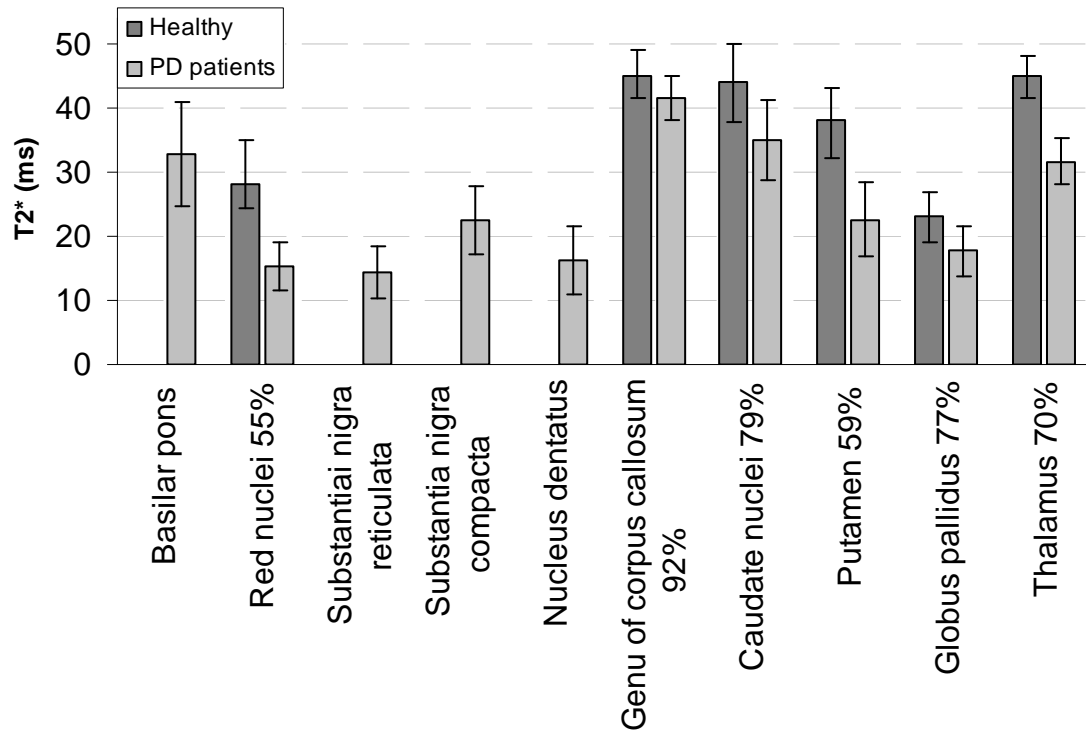
**Fig. 7.** Average $T_2$* in 51 patients with symptoms of PD, measured with the MapIt sequence, and in 12 healthy volunteers, measured with the QUTE sequence. The percentage differences are marked in appropriate structures.
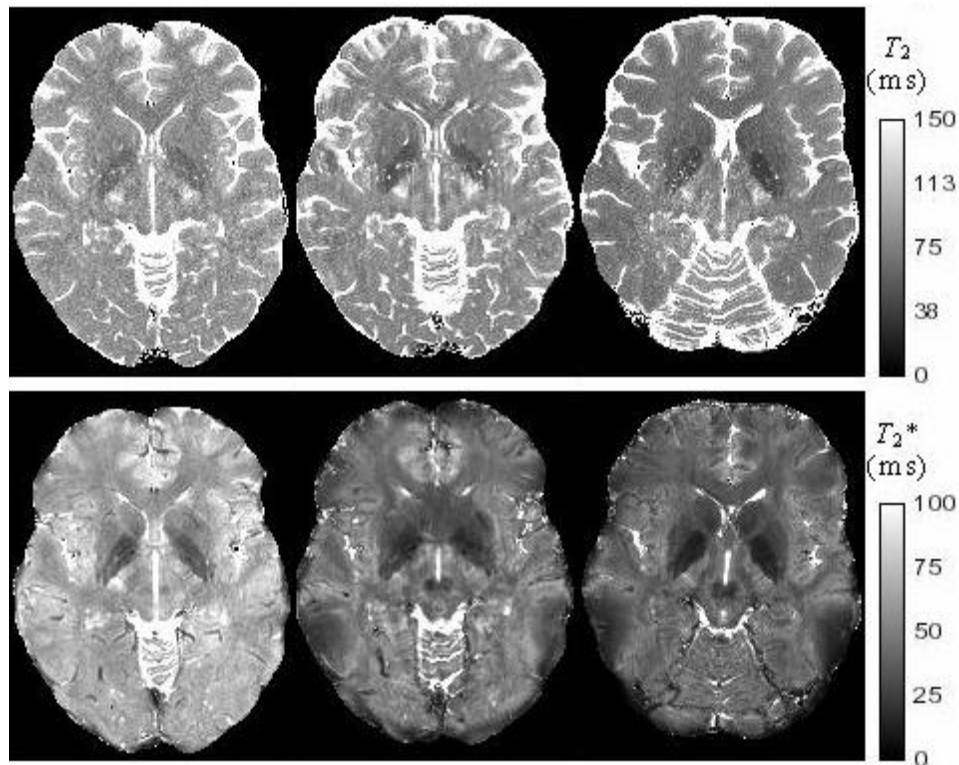


**Fig. 8.** The figure shows the field dependence of $T_2$ (top row) and $T_2$* (bottom row), increasing the field from 1.5 T (left column) to 3 T (middle column) and 4 T (right column). Modified from [Laurila 2007].

## 5.2.2. Contrast measurements

The decrease in longitudinal relaxation and the increase in transverse relaxation with main magnetic field is illustrated by parametric relaxation time maps in Fig. 3 (top row) for $T_1$ weighting and in Fig. 8 for $T_2$ and $T_2^*$ weighting [III].

In $T_2$-weighted TSE images of the MTBI patients, image contrast was not significantly affected by the increasing field strength from 1.5 T to 3 T, except in the globus pallidus. However, in the $T_2^*$-weighted GRE images, several but not all structures gained in their contrast measured against the genu of CC [IV].

In patients with symptoms of PD, contrast (measured against the genu of CC) was best in $T_2^*$ maps. Contrast measurements between different sequences were well intercorrelated but their relation to $T_2^*$ was dependent on the separation between WM and GM. Not only pure $T_2^*$ but also contrast of the qualitative images was capable of indicating the iron content of the extrapyramidal nuclei of the brain [V].

## 5.2.3. Histogram analysis

Whole-brain $T_1$ histograms, averaged over the 12 healthy volunteers, are shown in Fig. 9. Although only two maxima can be observed in the histograms, the three-Gaussian mixture model (d-f) was better suited to model the $T_1$ distribution than the two-Gaussian model (a-c) [III].

In the two-Gaussian mixture model, the intersection of the two Gaussian curves was considered as the WM-GM limit. The limit, however, resulted in excessive WM included within GM. Additionally, in the three-Gaussian model, the second intersection of the first and third peak as well as the centroid of the second peak – which was also considered the limit, hypothesizing that the partial volume effects would equally affect both WM and GM segmentation – included WM within the GM limits when the reasonability of the limits was assessed visually on the $T_1$ maps. In the three-Gaussian model, the first and third peaks were considered the WM and GM peaks, respectively, but the WM-GM limit was defined as the second intersection of the second and third Gaussian functions. Both the lower WM limit and the higher GM limit had to be decreased from those suggested by the widths of the Gaussian curves – the lower WM limit to include also short $T_1$ components of the WM and the higher GM limit to not include voxels affected by the partial volume effects of the CSF [III] .
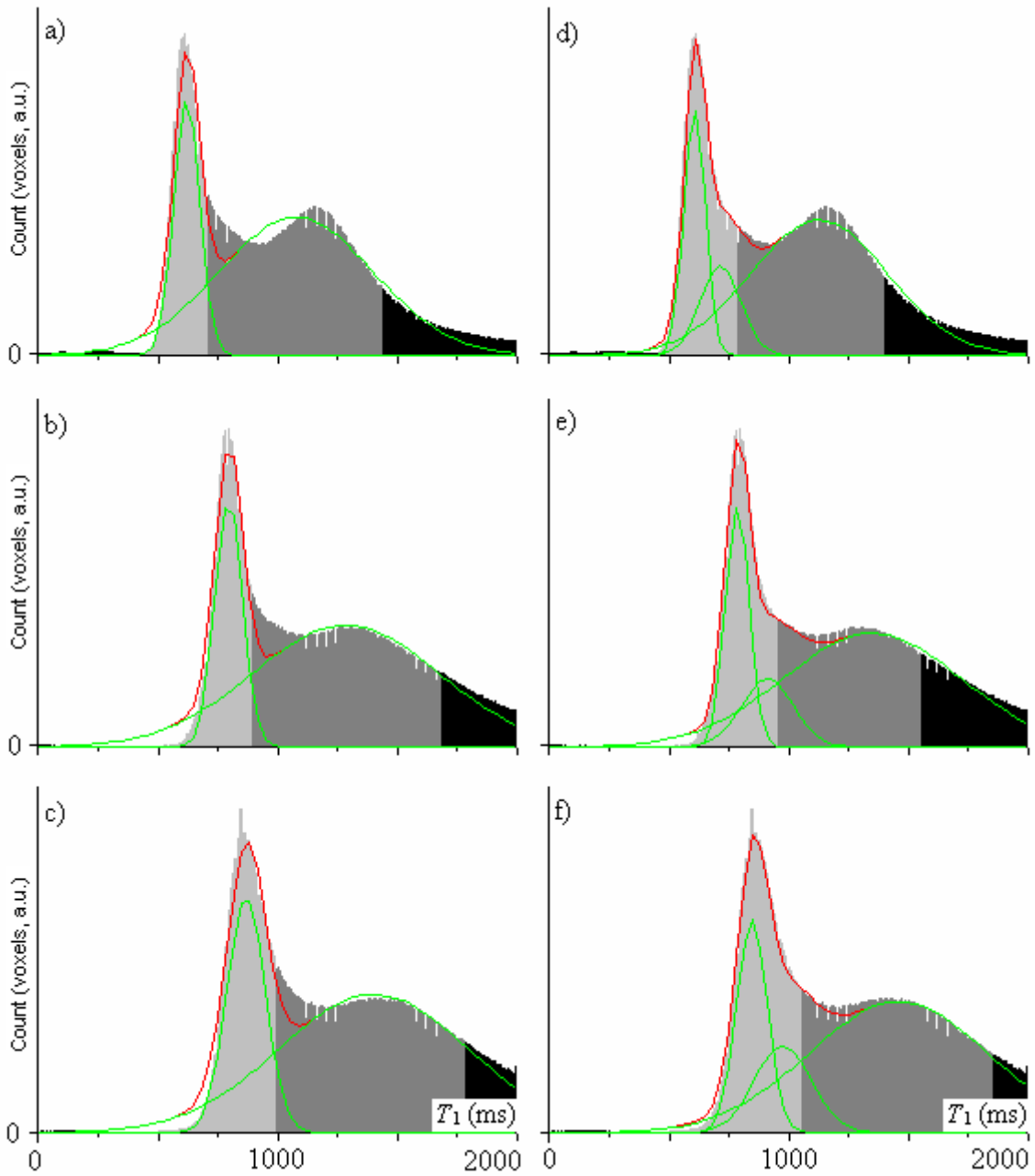
**Fig. 9.** The $T_1$ histograms of the whole brain averaged over the 12 healthy volunteers at 1.5 T, 3.0 T, and 4.0 T are shown in (a and d), (b and e), and (c and f), respectively. The histograms were fitted with a Gaussian mixture model using two (a-c) and three (d-f) Gaussians. The individual Gaussians are shown in a green line, and the red lines are their sum. The three-Gaussian model results in a smaller overall error than the two-Gaussian model at all fields. The light grey represents WM, the dark grey GM, and the black CSF. Their limits are defined by the Gaussian second intercept and peak width (two-Gaussian model) or by the values in Table 3 (three-Gaussian model) [Modified from Laurila 2007].

In the transverse relaxation times $T_2$ and $T_2{}^*$, the GM and WM peaks were not clearly separated (Fig. 10). At high fields, the peaks shifted to the left, i.e., towards faster relaxation. In addition, the peaks became slightly narrower and the $T_2{}^*$ distribution broadened to the left, indicating the improving contrast of some structures with respect to the whole brain. In particular, the $T_2$ values, except those of the red nuclei at 4.0 T, reduced along the left slope and their contrast improved at high fields.
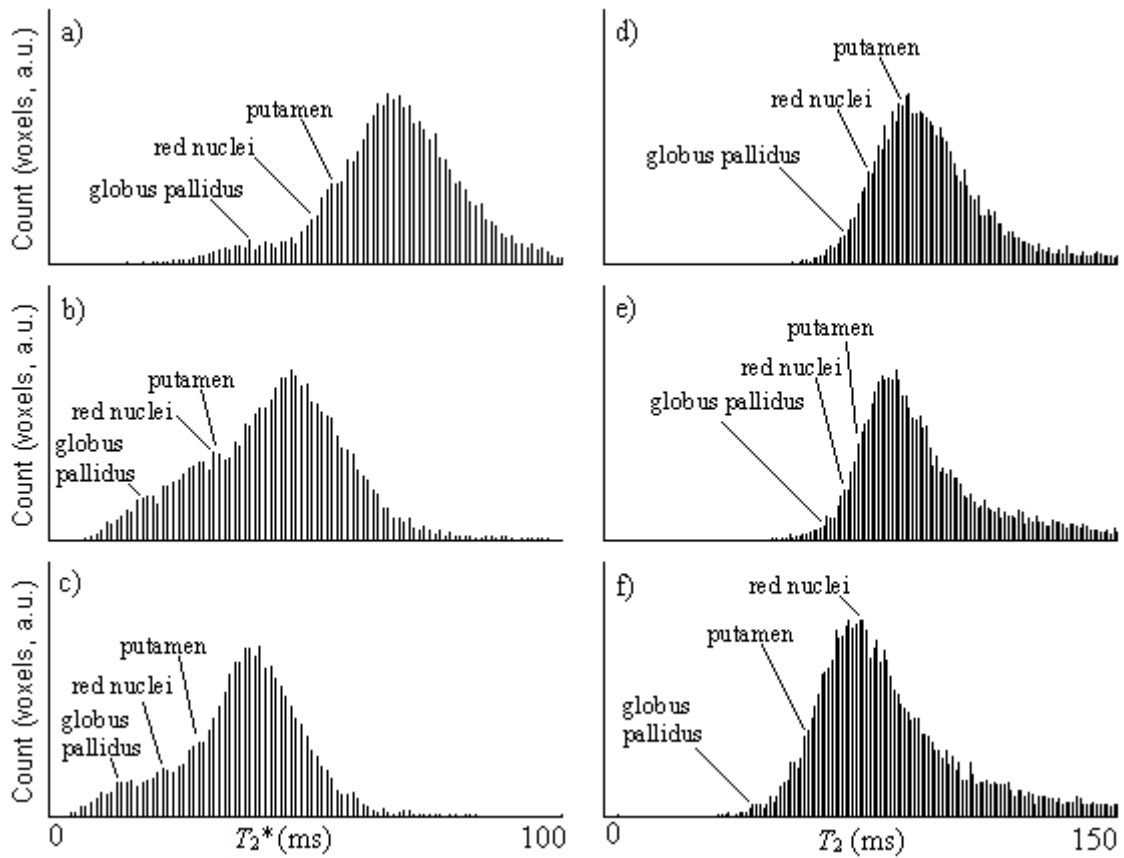


**Fig. 10.** $T_2{}^*$ and $T_2$ histograms through one slice of a healthy female volunteer. The relaxation times of individual structures are measured directly on the parametric maps and marked on the histograms. The $T_2{}^*$ histograms are shown in a), b), and c) and the $T_2$ histograms in d), e), and f) at 1.5 T, 3.0 T, and 4.0 T, respectively. [Modified from Laurila 2007]
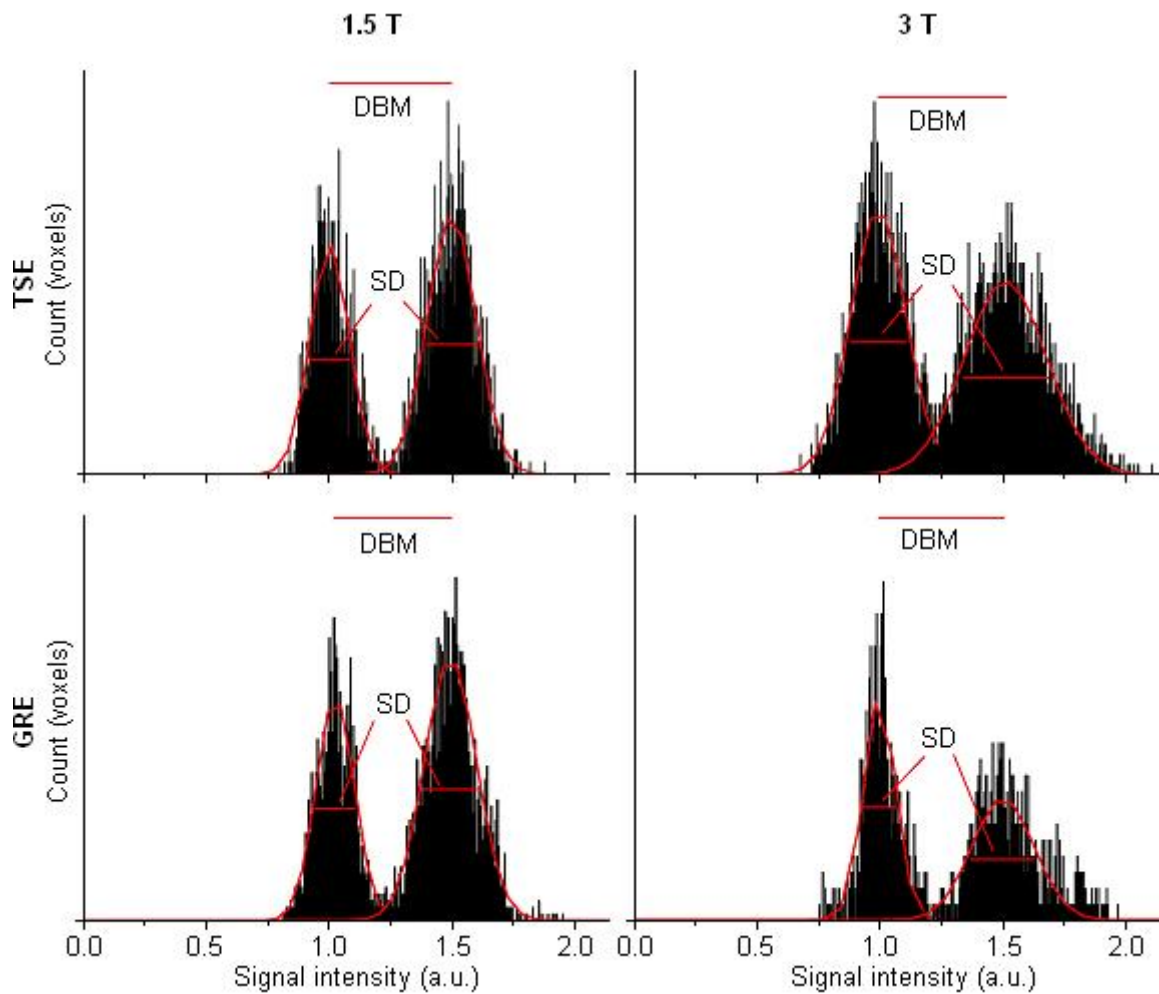
**Fig. 11.** Histograms in a turbo spin echo (TSE) image series (top row) and GRE image series (bottom row) in the genu of the corpus callosum and caudate nucleus averaged over the right and left hemispheres. The same representative patient is presented in the left column at 1.5 T and another patient is presented in the right column at 3 T. Gaussian fits are shown in red with difference between the means (DBM) and standard deviation (SD). Modified from [III].

In patients with MTBI, Gaussian fitting to several structures was performed. Peaks representing various structures, such as the caudate nuclei and genu of CC (Fig. 11), did not gain in separability with increasing field strength. Instead, in TSE, the wider peaks at 3 T than 1.5 T slightly decreased the average separability of the peaks [IV].

In patients with symptoms of PD, peak separability was measured similarly as in MTBI, but reversing the relation. FLAIR imaging was best compared to other sequences in separating adjacent structures [V].

# RESULTS

## 6. DISCUSSION

## 6.1. Segmentation

Segmentation of biological tissue was performed using different methods. For the segmentation of lymphomas in various locations of the body, manual and semiautomatic segmentation were used [I-II]. When segmenting regions of white and grey matter in the brain, the methods used were manual and automatic segmentation [III]. Segmentation proved to be reproducible but time consuming [I-II].

### 6.1.1. Segmentation techniques

Manual or semiautomatic segmentation, regardless of the application, is time consuming [I, II]. Therefore, these methods are poorly suited for clinical daily routine and are only used in carefully selected patients who clearly benefit from such analysis. Currently, there are new and improved automated software available for the volumetric analysis of multiple lymph nodes [Anders and Lell 2008]. However, in clinical routine, manual methods in one dimension only are still commonly used. For instance, the evaluation of treatment response of lymphomas relies on one-dimensional tumor measurements [Therasse *et al*. 2000, 2006].

It is clear that unless the object is perfectly regular in shape only full three-dimensional analysis can deliver accurate volumetric information. The more irregularly shaped the object, the larger the error in one- and two-dimensional analyses. Differences between 1-, 2-, and 3-dimensional measurements have been observed in breast cancer [Prasad *et al*. 2002], lung cancer [Tran *et al*. 2004], and lymphoma [Sohaib *et al*. 2000]. The response category may differ depending on the analysis method, especially between stable disease and partial response to treatment [Mazumdar *et al*. 2004] or stable disease and progressive disease [Tran *et al*. 2004]. In this study, reasonable agreement between 1-, 2-, and 3-dimensional analyses was found, but there was some deviation between partial response, stable disease, and progressive disease [I, II]. These differences arise especially in irregularly shaped tumors and tumors changing shape during therapy [Mazumdar *et al*. 2004].

MRI has been previously found to be more sensitive in tumor detection than CT [Lumachi *et al*. 2006]. Indeed, in our results, the tumor volume derived from MRI was often larger than the volume derived from CT (slope 0.59) [II]. Additionally, in CT, there were false-negative results, which were verified after the blind image analysis

[Rossi *et al*. 2010b]. False-positive errors in segmentation can be minimized by landmarking and segmenting out various structures prior to tumor delineation [Rangayyan *et al*. 2008 and 2009, Banik *et al*. 2008 and 2010]. To further increase sensitivity in tumor detection, functional and metabolic imaging methods are suggested for the early monitoring of treatment response. Because combined PET-CT becomes increasingly available for daily clinical routine, it should be noted that this combination is more sensitive than conventional MRI for lymph node detection [Schmidt *et al*. 2007]. Semiautomated volumetry has been used recently with fused PET-CT images to calculate metabolic tumor volume [Lichy *et al*. 2007; Wu *et al*. 2011a and 2011b]. PET shows the disappearance of lymphatic tissue where conventional MRI still shows scar tissue [Rossi *et al*. 2011].

It is also possible to assess molecular information using MR imaging methods. DWI and MRS have already shown promising correlation with the early treatment response of lymphomas [Harry *et al.* 2010, Wu *et al*. 2011b]. Even morphological imaging showed usefulness in treatment response monitoring, provided imaging was performed at an early stage [I, II]. Besides adjusting the time of imaging, the use of whole-body diffusion imaging may provide MRI advantages over PET-CT [Schmidt *et al*. 2010]. DWI-based volumetry, at least in post-therapy assessment, has proved to be more accurate than volumetry in conventional MR images [Curvo-Semedo *et al*. 2011]. Furthermore, it has been suggested that visual estimations of DW images may suffice for post-therapy imaging and the time-consuming volumetric measurements might not be necessary [Curvo-Semedo *et al*. 2011].

Functional and molecular information correlates with volumetry not only in lymphomas but in several other tissues as well. In the brain, these include correlations between brain infarction volume and DTI values [Rossi *et al*. 2010a] and FLAIR lesion volume and biomarkers in multiple sclerosis [Hagman *et al*. 2011]. Tissue segmentation can be supported with histogram analysis. In WM-GM segmentation, histograms can be used in deciding the limits for $T_1$ values [Rooney *et al*. 2007]; the decision can be aided with prior knowledge in their distribution over the brain [III]. Visual inspection is still required for judging the appropriateness of the chosen limits.

Furthermore, the possibility should be considered as to whether leaving out a small portion of pixels between WM and GM [Rooney *et al*. 2007] would improve the segmentation in terms of minimizing partial volume effects. This approach in whole-brain segmentation may also help in ruling out some grey matter structures, such as the thalamus, from being classified as white matter due to signal inhomogeneities. Such inhomogeneities affect the quality of the final $T_1$ map in parametric fitting [III]. However, user interference might be needed to prevent unintentional exclusion of structures such as the thalamus from segmentation.

## 6.1.2. Clinical correlation

Standard methods for response monitoring classify the response using percentage volume reduction [Miller *et al.* 1981, Therasse *et al.* 2000, 2006]. Our results suggest that it may also be worth considering using absolute volumes and changes in the same [I, II]. Absolute volume changes may better correlate with clinical data because in several cases they have combined information on both the volume reduction and the initial tumor volume. Publications I and II were, to my knowledge, the first morphological studies at such an early stage of NHL treatment in the literature.

Early response monitoring of the treatment of lymphomas has previously been performed with PET [MacManus *et al.* 2007, Lucignani 2007, Römer *et al.* 1998], whereas morphological imaging has mainly been performed pre- and post-treatment only [Rodriguez 1998]. In the literature, there are different results on whether pre- and post-treatment volume does [Willett *et al.* 1988, Smith *et al.* 1998] or does not [Rodriguez 1998] correlate with the possibility to relapse. In this study, no connection was found [I, II].

Large remaining tumor volumes at the completion of treatment were predictive of higher mortality [II]. The increasing mortality with faster tumor volume decrease in MRI after only one week of chemotherapy was not statistically proven [I] and should therefore be re-evaluated with larger and more homogeneous patient data. Our different results between MRI and CT [I, II] due to only slightly different patient populations raise the question regarding whether this was a randomly found result; furthermore, the 1- and 2-dimensional measurements of the same patients did not support the finding. This question is further emphasized by the lack of an explanation to the MRI finding, such as an association with mortality or tumor malignancy. It needs to be clarified if individual tolerance of drug doses can explain the finding. This would suggest modifying treatment planning.

The results are affected by the size and inhomogeneity of the patient population. The larger initial tumor volume of relapsed lymphomas compared with previously untreated cases is one example of the diversity within the sample. We are currently expecting new results from an ongoing study at Tampere University Hospital with new patient recruitment.

## 6.2. Signal analysis

Signal analysis included studying the signal changes due to sequence design, magnetic field strength, and tissue properties. In parametric relaxation time mapping, the signal intensities of a time series were fitted with relaxation curves. In several cases. the signal or parameter was analyzed using histograms, whether hidden or visible.

### 6.2.1. Field strength

Several clinical scanners are being updated from 1.5 T to 3 T at times of new inventories, with the only main limitation to this development being the costs. In scientific use, the field strengths are much higher and ever increasing [Rooney *et al*. 2007]. In this study, three different field strengths were compared [III, IV]. Image quality improved from 1.5 T to 3 T [III, IV]. At 4 T, there was potential for further improvements; however, the increasing signal intensity was not in full use due to RF coil inhomogeneities at the time of the measurements [III].

Along with several other advantages and disadvantages of high fields, increasing susceptibility may be both advantageous and disadvantageous [Duggan-Jahns 2008]. Although artefacts arise in locations such as air-tissue interfaces, SWI gains in terms of improved contrast [Pinker *et al*. 2007, Duggan-Jahns 2008]. Prior knowledge on field dependence states that, in SWI, iron-containing structures, veins, and lesions gain contrast at high fields due to increased phase shift [Pinker *et al*. 2007]. In this study, the PD patients were imaged at a single field strength only [V]. After minimum intensity projection, the contrast of iron-containing structures and the visibility of veins were excellent with 3-T imaging.

The visibility of veins and other small structures has further improved at ultra-high fields because improvements in SNR allow for better spatial resolution [Barth *et al*. 2003]. In $T_2$- and $T_2$*-based images, the improvement in contrast was considerable in iron-containing structures but modest elsewhere [III, IV]. The visualization of not only the extrapyramidal nuclei containing ferritin but also the iron in the veins was improved. Although the effects were pronounced in iron-containing structures, a slight overall decrease in not only $T_2$* but also $T_2$ was evident in the whole brain parenchyma [III]. This field dependence is a result of water diffusion in the field-dependent susceptibility-induced gradients and chemical exchange of protons between molecular binding sites with different chemical shifts [Bartha *et al*. 2002]. Both of these mechanisms lead to field-dependent rate of spin dephasing due to a change in the Larmor frequency of a proton.

In $T_1$-weighted images, no significant contrast improvements are expected with increasing main magnetic field [Rooney *et al*. 2007]; instead, contrast may even decline [Fischer *et al*. 1990]. In this study, the peak-to-peak contrast of parametric $T_1$ maps remained at an approximately constant level [III]. The GM and WM peaks in the

histograms did slightly merge when increasing the main magnetic field. The convergence may partly derive from the RF inhomogeneities, experienced especially at 4 T, slightly affecting the $T_1$ values. The $T_1$ values of WM and GM may appear merged especially in the thalamus and the splenium of corpus callosum in the central image and the WM and cortical GM in the left frontal lobe. Nevertheless, the expected increase in $T_1$ with field strength was observed in all volunteers. Although the increase may not affect the contrast of conventional $T_1$-weighted MRI, prolonged $T_1$ enables improved contrast in selected applications. For example, in angiographic MRI the background suppression is improved due to greater differences between the relaxation times of blood and the brain parenchyma [Campeau *et al.* 2001]. Field-dependent improvement in contrast is also observed in magnetization transfer imaging [Pohmann *et al.* 2011].

## 6.2.2. Sequence comparison

At a given field strength, relaxation times are, in principle, quantitative. However, the measurements depend on several issues, such as the MRI scanner hardware and software, the imaging sequence, the correction for inhomogeneities, and the curve-fitting procedure. Consequently, agreement between different studies may be poor [Rooney *et al.* 2007]. Therefore, in the $T_2$* maps of this study, a comparison between healthy volunteers, imaged with the QUTE imaging sequence [III], and the patients with symptoms of Parkinson's disease, imaged with the MapIt sequence [V], is not appropriate. Indeed, previous studies have shown a significant decrease in $T_2$* in the substantia nigra [Martin *et al.* 2008]; however, as shown by the percentages in Fig. 7, a decrease from QUTE to MapIt is observed in all brain structures, including those unaffected by PD. Therefore, the overall decrease between the sequences cannot be considered to originate from the disease.

It may thus be assumed that either the QUTE sequence overestimates or the MapIt sequence underestimates $T_2$*, especially in iron-containing brain structures, i.e., structures with short $T_2$*. The MapIt sequence was originally designed to image cartilage [Hughes *et al.* 2007; Welsch *et al.* 2008 and 2010] where iron, with its short $T_2$*, does not need to be considered. In Fig. 7, the genu of corpus callosum is less differentiated between the sequences than other structures. In the table, the genu of CC is the only structure with no significant iron accumulation [Hallgren and Sourrander 1958]. At 3 T, QUTE allows for rapid sampling with echo spacing of 3.4 ms, compared to 7.1 ms in MapIt. Additionally, the number of echoes is superior in QUTE compared to MapIt. Furthermore, QUTE also allows for very long effective *TR* to improve SNR [Dierkes *et al.* 2004]. Finally, the shimming method performed prior to QUTE was based on individual adjustments according to the subject, whereas that prior to MapIt was only based on the manufacturer's adjustments at the time of installing the scanner. Based on these differences in the sequence design and scanner adjustments, the values measured with the QUTE sequence are probably closer to the "absolute truth" than those

measured with the MapIt sequence; this view is also supported by $T_2^*$ values published in the literature [Martin *et al*. 2008].

Whereas QUTE was observed to be a fast and reliable tool for $T_2^*$ mapping in the brain, TAPIR was reasonably reliable but not fast [III]. For diagnostic purposes, various sequences other than relaxation time mapping need to be acquired, and thus imaging sequences need to be rapid. The problem with TAPIR is that during its typical acquisition time of 3 to 8 min [Zaitsev *et al*. 2003], only approximately 14 slices can be measured. This sequence must also be accompanied with a 1-min inversion efficiency mapping. For full brain coverage, these sequences are repeated two or three times at different locations, resulting in long measurement times. Thus, alternative sequences for $T_1$ mapping have been considered, such as a variation of QUTE with different flip angle and *TR* [Neeb *et al*. 2008].

Although there are several parameters affecting $T_2$- and $T_2^*$-weighted images, they are strongly dependent on transverse relaxation [Hornak 1996]. Therefore, it is not surprising that the qualitative signal or contrast of the $T_2$- and $T_2^*$-weighted images are also correlated with quantitative $T_2^*$ [V]. Instead, no explanation was found as to why the relation between quantitative $T_2^*$ and $T_2$- or $T_2^*$-weighted images was dependent on the tissue type, i.e., the separation between WM and GM. Possible explanations include incomplete $T_1$ relaxation, low water content in WM compared to GM, and differences between $T_2$ and $T_2^*$. However, none of the above possibilities alone is sufficient to provide an acceptable explanation.

### 6.2.3. Histogram analysis

Histogram analysis can be easily performed with gray-scale MR images. Several basic measurements, such as the measurement of the mean and SD in a given ROI, are implicitly based on histograms, although in the software the histograms are usually hidden from the user. In multiple sclerosis, such analysis is often performed in MTR images, where peak height, peak position, and average MTR are of interest [Filippi and Rocca 2007]. Peak height reflects the brain volume [van Buchem *et al*. 1996], but it was not used in this study. Histograms can also be used in gray-scale-based segmentation [Heinonen *et al*. 1998a] and contrast enhancement when windowing images on medical displays for diagnosis. Depending on the software, the histogram may be hidden (Anatomatic$^{TM}$) or visible (ImageJ) during the adjustments of windowing and threshold setting.

Histograms can be used in segmentation in a manner that they are visible to the user during the whole procedure. Based on both visual assessment and curve fitting, the signal distribution of grey and white matter [III] and small structures [IV] quite often obeyed Gaussian distribution in this thesis. Detailed histogram analysis using Gaussian fitting can be used to aid when discriminating between tissues. Besides prior knowledge,

the histogram-based decision on the segmentation limits between WM and GM was based on averaging all patients' data. Had the segmentation limits been decided for each volunteer individually, the result might have been different due to individual distributions of $T_1$ values.

The distinction between various tissues in the images and histograms is influenced by several factors, including tissue properties. Although not straightforward, $T_1$ is largely dependent on tissue water content [Neeb et al. 2006]. Because the water content of WM is significantly lower than that of GM, there is a clear separation between the GM and WM peaks in both water content [Neeb et al. 2006] and $T_1$ [III] histograms. In addition, in WM, the cholesterol contained in myelin enhances $T_1$ relaxation through magnetization transfer, which further highlights the separation between the $T_1$ values of WM and GM [Koenig 1991]. Instead of depending on the myelin content of WM structures, transverse relaxation is more affected by the high iron content in deep GM structures. Thus, the transverse relaxation of these GM structures is faster compared to WM, whereas – as in $T_1$ relaxation – cortical GM protons relax slower than WM protons. Therefore, the peaks of grey and white matter lose separability in a way that disables histogram-based segmentation in $T_2$ and $T_2$* images [III, IV].

The reproducibility of histograms is usually very good [Sormani et al. 2000]. However, ROI localization affects the result of quantitative image analysis. Excluding peripheral voxels from the ROI to avoid partial volume effects is one approach to overcome this problem. Not only the ROI setting but also the voxel size can affect MRI results of specific applications. The effect of voxel size can, for example, be observed as underestimated fractional anisotropy in DTI images with anisotropic voxel size [Oouchi et al. 2007]. For good reproducibility and accurate measurements, both good anatomical knowledge and careful ROI setting must be assured.

### 6.2.4. Iron content

Paramagnetic substances, such as ferrous iron compounds, are present in various structures of the brain [Hallgren and Sourander 1958]. These induce strong susceptibility gradients that enhance spin dephasing. Iron deposits have been measured by MRI using $T_2$ mapping [Gossuin et al. 2004], $T_2$* mapping [Martin et al. 2008], FDRI [Pfefferbaum et al. 2009], phase mapping [Haacke et al. 2009b], and susceptibility mapping [Lotfipour et al. 2011]. Unlike in previous studies, in this study, the putative iron content was correlated not only with quantitative imaging, which in this case were the $T_2$* maps, but also with standard clinical images: SWI, $T_2$-weighted images, and FLAIR images [V]. The correlation of iron content with clinical images was not worse than that with quantitative images, suggesting that iron measurements be applicable not only in scientific studies but also in clinical environments. In addition to the methods described above, mapping of pure susceptibility has been suggested that is less sensitive to error than phase maps [Shmueli et al. 2009].

In normal aging, ferrous iron compounds are known to accumulate in each of the structures listed in Fig. 7, except for the genu of corpus callosum [Hallgren and Sourander 1958]. In Parkinson's disease, excessive accumulation is measured in the substantia nigra [Dexter *et al*. 1991, Youdim and Riederer 1993, Antonini *et al*. 1993, Ryvlin *et al*. 1995, Vymazal *et al*. 1999, Griffiths *et al*. 1999, Graham *et al*. 2000, Kosta *et al*. 2006, Martin *et al*. 2008, Brar *et al*. 2009, Zhang J *et al*. 2010]. Enhanced spin dephasing was measured in the current thesis with various sequences [V]. A comparison with healthy volunteers on the same scanner and sequence as those used in patients with Parkinson's disease, along with a two-year follow-up of the patients, will be helpful and will be reported in an ongoing study at the Tampere University Hospital.

### 6.2.5.  Future trends

This study was mainly a technical consideration of methods and devices that are currently used – or have the potential for future use – in clinical environments. However, we are currently working on their clinical correlation. In particular, the putative iron content is in focus because increased iron content in the brain is associated with both normal aging and several neurodegenerative diseases. Iron quantification has great future potential because it correlates with various MRI methods, including not only quantitative $T_2$, $T_2$*, and susceptibility mapping but also qualitative clinical images, such as $T_2$-weighted imaging or SWI. This potential may be expected to be fully exploited due to the current interest in both advanced imaging methods, including susceptibility mapping, and their clinical applications in various neurodegenerative diseases in several leading research facilities worldwide. Perhaps with the increasing knowledge on the dynamics of iron accumulation, it may appear as an early sign of neurodegenerative diseases and may be used in early treatment decisions.

## 7. CONCLUSIONS

Both qualitative and quantitative MR images used in this study were of high quality and were capable of delivering fine resolution, without compromising signal-to-noise ratio. Segmentation, histogram analysis, and parametric fitting were reproducible, though the first two methods were slightly affected by user interference.

The *in vivo* relaxation times measured in this study showed clear field dependence. The longitudinal relaxation time became longer, whereas the transverse relaxation time became shorter. Both of these changes in relaxation times are beneficial for different contrast mechanisms at ultra-high fields.

In lymphomas, the correlation between segmentation results and clinical characteristics suggested using absolute volume changes in addition to percentage changes. In Parkinson's disease, the signal changes correlated with iron deposits in both parametric maps and ordinary clinical MR images. This method might be useful as an early marker of disease progression.

**REFERENCES**

Anders K, Lell M. 2008. Identification of a non-Hodgkin lymphoma recurrence using the SOMATOM definition AS+ for evaluation in oncology routine. SOMATOM Sessions, May 2008: p.40-41. http://www.siemens.com/healthcare-magazine

Antonini A, Leenders KL, Meier D, Oertel WH, Boesiger P, Anliker M. 1993. $T_2$ relaxation time in patients with Parkinsons disease. Neurology. 1993;43:697-700.

Atkins MS, Mackiewich BT. 1998. Fully automatic segmentation of the brain in MRI. IEEE Trans Med Imaging. 1998;17:98-107.

Banik S, Rangayyan RM, Boag GS. 2008. Landmarking of computed tomographic images to assist in segmentation of abdominal tumors caused by neuroblastoma. Conf Proc IEEE Eng Med Biol Soc. 2008;2008:3126-3129.

Banik S, Rangayyan RM, Boag GS. 2010. Automatic segmentation of the ribs, the vertebral column, and the spinal canal in pediatric computed tomographic images. J Digit Imaging. 2010;23:301-322.

Barth M, Nöbauer-Huhmann IM, Reichenbach JR, Mlynárik V, Schöggl A, Matula C, Trattnig S. 2003. High-resolution three-dimensional contrast-enhanced blood oxygenation level-dependent magnetic resonance venography of brain tumors at 3 Tesla: first clinical experience and comparison with 1.5 Tesla. Invest Radiol. 2003;38:409-414.

Bartha R, Michaeli S, Merkle H, Adriany G, Andersen P, Chen W, Ugurbil K, Garwood M. 2002. In vivo 1H2O T2+ measurement in the human occipital lobe at 4T and 7T by Carr-Purcell MRI: detection of microscopic susceptibility contrast. Magn Reson Med. 2002;47:742-750.

Berg D. 2007. Disturbance of iron metabolism as a contributing factor to SN hyperechogenicity in Parkinson's disease: implications for idiopathic and monogenetic forms. Neurochem Res. 2007;32:1646-1654.

Bloch F, Hansen WW, Packard ME. 1946. Nuclear induction. Phys Rev. 1946;69:679-680.

Bloch F. 1946. Nuclear induction. Phys Rev. 1946;70:460-474.

Brar S, Henderson D, Schenck J, Zimmerman EA. 2009. Iron accumulation in the substantia nigra of patients with Alzheimer disease and parkinsonism. Arch Neurol. 2009;66:371-374.

Bryant RG. 1996. The dynamics of water-protein interactions. Annu Rev Biophys Biomol Struct. 1996;25:29-53.

Bryant RG, Korb JP. 2005. Nuclear magnetic resonance and spin relaxation in biological systems. Magn Reson Imaging. 2005;23:167-173.

van Buchem MA, McGowan JC, Kolson DL, Polansky M, Grossman RI. 1996. Quantitative volumetric magnetization transfer analysis in multiple sclerosis: estimation of macroscopic and microscopic disease burden. Magn Reson Med 1996;36:632– 636.

Campeau NG, Huston J 3rd, Bernstein MA, Lin C, Gibbs GF. 2001. Magnetic resonance angiography at 3.0 Tesla: initial clinical experience. Top Magn Reson Imaging. 2001;12:183-204.

Carr HY, Purcell EM. 1954. Effects of diffusion free precession in nuclear magnetic resonance experiments. Phys Rev. 1954;94:630-638.

Castellano G, Bonilha L, Li LM, Cendes F. 2004. Texture analysis of medical images. Clin Radiol. 2004;59:1061-1069.

Catana C, Wu Y, Judenhofer MS, Qi J, Pichler BJ, Cherry SR. 2006. Simultaneous acquisition of multislice PET and MR images: initial results with a MR-compatible PET scanner. J Nucl Med. 2006;47:1968-1976.

Chávez FV, Halle B. 2006. Molecular basis of water proton relaxation in gels and tissue. Magn Reson Med. 2006;56:73-81.

Chen JC, Hardy PA, Kucharczyk W, Clauberg M, Joshi JG, Vourlas A, Dhar M, Henkelman RM. 1993. MR of human postmortem brain tissue: correlative study between $T_2$ and assays of iron and ferritin in Parkinson and Huntington disease. AJNR Am J Neuroradiol. 1993;14:275-281.

Cohen BA, Inglese M, Rusinek H, Babb JS, Grossman RI, Gonen O. 2007. Proton MR spectroscopy and MRI-volumetry in mild traumatic brain injury. AJNR Am J Neuroradiol. 2007;28:907-913.

Curvo-Semedo L, Lambregts DM, Maas M, Thywissen T, Mehsen RT, Lammering G, Beets GL, Caseiro-Alves F, Beets-Tan RG. 2011. Rectal Cancer: Assessment of Complete Response to Preoperative Combined Radiation Therapy with Chemotherapy--Conventional MR Volumetry versus Diffusion-weighted MR Imaging. Radiology. 2011;260:734-743.

Dexter DT, Carayon A, Javoy-Agid F, Agid Y, Wells FR, Daniel SE, Lees AJ, Jenner P, Marsden CD. 1991. Alterations in the levels of iron, ferritin and other trace metals in Parkinson's disease and other neurodegenerative diseases affecting the basal ganglia. Brain. 1991;114:1953-1975.

Dierkes T, Neeb H, Shah NJ. 2004. Distortion correction in echo-planar imaging and quantitative $T_2$* mapping. Proceedings of the international workshop on quantitation in biomedical imaging with PET and MRI. Int Congr Ser. 2004;1265:181–185.

Dodin P, Pelletier JP, Martel-Pelletier J, Abram F. 2010. Automatic Human Knee Cartilage Segmentation from 3D Magnetic Resonance Images. IEEE Trans Biomed Eng. 2010 Jul 15.

Drayer B, Burger P, Darwin R, Riederer S, Herfkens R, Johnson GA. 1986. MRI of brain iron. AJR. 1986;147:103-110.

Duggan-Jahns T. 2008. The Evolution of Magnetic Resonance Imaging: 3T MRI in Clinical Applications. http://www.eradimaging.com/site/article.cfm?ID=426 [Referred 15.8.2011]

Ebel A, Maudsley AA. 2005. Detection and correction of frequency instabilities for volumetric 1H echo-planar spectroscopic imaging. Magn Reson Med. 2005;53:465-469.

Ebel A, Maudsley AA, Schuff N. 2007. Correction of local B0 shifts in 3D EPSI of the human brain at 4 T. Magn Reson Imaging. 2007;25:377-380.

Erez AB, Rothschild E, Katz N, Tuchner M, Hartman-Maeir A. 2009. Executive functioning, awareness, and participation in daily life after mild traumatic brain injury: a preliminary study. Am J Occup Ther. 2009;63:634-640.

Filippi M, Rocca MA. 2007. Magnetization transfer magnetic resonance imaging of the brain, spinal cord, and optic nerve. Neurotherapeutics. 2007;4:401-413.

Filler AG, Tsuruda JS, Richards TL, Howe FA. 1992. Images, apparatus, algorithms and methods. GB9216383.1, UK Patent Office, 1992.

Finnish Cancer Registry - Institute for Statistical and Epidemiological Cancer Research: Cancer Incidence in Finland 2006 and 2007. Cancer Statistics of the National Institute for Health and Welfare (THL). Cancer Society of Finland Publication No. 76. Helsinki 2009.

Fischer HW, Rinck PA, Van Haverbeke Y, Muller RN. 1990. Nuclear relaxation of human brain gray and white matter: analysis of field dependence and implications for MRI. Magn Reson Med. 1990;16:317-334.

Fitzgerald DB, Crosson BA. 2011. Diffusion weighted imaging and neuropsychological correlates in adults with mild traumatic brain injury. Int J Psychophysiol. 2011 Feb 19.

Franck JM, Demas V, Martin RW, Bouchard LS, Pines A. 2009. Shimmed matching pulses: simultaneous control of rf and static gradients for inhomogeneity correction. J Chem Phys. 2009;131:234506.

Gao X, Xue Z, Xing J, Lee DY, Gottschalk SM, Heslop HE, Bollard CM, Wong ST. 2010. Computer-assisted quantitative evaluation of therapeutic responses for lymphoma using serial PET/CT imaging. Acad Radiol. 2010;17:479-488.

Goetz P, Blamire A, Rajagopalan B, Cadoux-Hudson T, Young D, Styles P. 2004. Increase in apparent diffusion coefficient in normal appearing white matter following human traumatic brain injury correlates with injury severity. J Neurotrauma. 2004;21:645-654.

Gosselin N, Bottari C, Chen JK, Petrides M, Tinawi S, de Guise E, Ptito A. 2011. Electrophysiology and functional MRI in post-acute mild traumatic brain injury. J Neurotrauma. 2011;28:329-341.

Gossuin Y, Muller RN, Gillis P. 2004. Relaxation induced by ferritin: a better understanding for an improved MRI iron quantification. NMR Biomed. 2004;17:427-432.

Govind V, Gold S, Kaliannan K, Saigal G, Falcone S, Arheart KL, Harris L, Jagid J, Maudsley AA. 2010. Whole-brain proton MR spectroscopic imaging of mild-to-moderate traumatic brain injury and correlation with neuropsychological deficits. J Neurotrauma. 2010;27:483-496.

de Graaf RA, Brown PB, McIntyre S, Nixon TW, Behar KL, Rothman DL. 2006. High magnetic field water and metabolite proton $T_1$ and $T_2$ relaxation in rat brain in vivo. Magn Reson Med. 2006;56:386-394.

Graham JM, Paley MN, Grünewald RA, Hoggard N, Griffiths PD. 2000. Brain iron deposition in Parkinson's disease imaged using the PRIME magnetic resonance sequence. Brain. 2000;12:2423-2431.

Griffiths PD, Dobson BR, Jones GR, Clarke DT. 1999. Iron in the basal ganglia in Parkinson's disease. An in vitro study using extended X-ray absorption fine structure and cryo-electron microscopy. Brain. 1999;122:667-673.

Gröhn HI, Michaeli S, Garwood M, Kauppinen RA, Gröhn OH. 2005. Quantitative $T_1$(rho) and adiabatic Carr-Purcell $T_2$ magnetic resonance imaging of human occipital lobe at 4 T. Magn Reson Med. 2005;54:14-19.

Haacke EM, Xu Y, Cheng YC, Reichenbach JR. 2004. Susceptibility weighted imaging (SWI). Magn Reson Med. 2004;52:612-618.

Haacke EM, Mittal S, Wu Z, Neelavalli J, Cheng YC. 2009a. Susceptibility-weighted imaging: technical aspects and clinical applications, part 1. Am J Neuroradiol. 2009;30:19-30.

Haacke EM, Makki M, Ge Y, Maheshwari M, Sehgal V, Hu J, Selvan M, Wu Z, Latif Z, Xuan Y, Khan O, Garbern J, Grossman RI. 2009b. Characterizing iron deposition in multiple sclerosis lesions using susceptibility weighted imaging. J Magn Reson Imaging. 2009;29:537–544.

Haacke EM, Duhaime AC, Gean AD, Riedy G, Wintermark M, Mukherjee P, Brody DL, DeGraba T, Duncan TD, Elovic E, Hurley R, Latour L, Smirniotopoulos JG, Smith DH. 2010a. Common data elements in radiologic imaging of traumatic brain injury. J Magn Reson Imaging. 2010;32:516-543.

Haacke EM, Miao Y, Liu M, Habib CA, Katkuri Y, Liu T, Yang Z, Lang Z, Hu J, Wu J. 2010b. Correlation of putative iron content as represented by changes in $R_2$* and phase with age in deep gray matter of healthy adults. J Magn Reson Imaging. 2010;32:561-576.

Hagman S, Raunio M, Rossi M, Dastidar P, Elovaara I. 2011. Disease-associated inflammatory biomarker profiles in blood in different subtypes of multiple sclerosis: prospective clinical and MRI follow-up study. J Neuroimmunol. 2011;234:141-147.

Hallgren B, Sourander P. 1958. The effect of age on the non-haemin iron on in the human brain. J. Neurochem. 1958;3:41-51.

Hahn EL. 1950. Spin Echoes. Phys Rev. 1950;80:580-594.

Halle B. 2006. Molecular theory of field-dependent proton spin-lattice relaxation in tissue. Magn Reson Med. 2006;56:60-72.

Harry VN, Semple SI, Parkin DE, Gilbert FJ. 2010. Use of new imaging techniques to predict tumour response to therapy. Lancet Oncol. 2010;11:92-102.

Heinonen T, Dastidar P, Kauppinen P, Malmivuo J, Eskola H. 1998a. Semi-automatic tool for segmentation and volumetric analysis of medical images. Med Biol Eng Comput. 1998;36:291-296.

Heinonen T, Dastidar P, Eskola H, Frey H, Ryymin P, Laasonen E. 1998b. Applicability of semi-automatic segmentation for volumetric analysis of brain lesions. J Med Eng Technol. 1998;22:173-178.

Heussel CP, Meier S, Wittelsberger S, Götte H, Mildenberger P, Kauczor HU. 2007. Follow-up CT measurement of liver malignoma according to RECIST and WHO vs. volumetry. Rofo. 2007;179:958-964.

Holli KK, Harrison L, Dastidar P, Waljas M, Liimatainen S, Luukkaala T, Ohman J, Soimakallio S, Eskola H. 2010. Texture analysis of MR images of patients with Mild Traumatic Brain Injury. BMC Med Imaging. 2010;10:8.

Hornak JP. 1996. The Basics of MRI. [Referred Aug 3rd 2011] http://www.cis.rit.edu/htbooks/mri/index.html

Howe KR. 1988. Against the quantitative-qualitative incompatibility thesis or dogmas die hard. Educational Researcher. 1988;17:10–16.

Hughes T, Welsch GH, Trattnig S, Brandi L, Domayer S, Mamisch TC. 2007. $T_2$-star Relaxation as a means to diffrentiatie Cartilage Repair Tissue after Microfracturing Therapy. Proc. ISMRM 2007;15:183.

Johnson GA, Herfkens RJ, Brown MA. 1985. Tissue relaxation time: *in vivo* field dependence. Radiology. 1985;156:805-810.

Koenig SH, Schillinger WE. 1969. Nuclear magnetic relaxation dispersion in protein solutions. I. Apotransferrin. J Biol Chem. 25;244:3283-3289.

Koenig SH, Brown RD 3rd, Adams D, Emerson D, Harrison CG. 1984. Magnetic field dependence of $1/T_1$ of protons in tissue. Invest Radiol. 1984;19:76-81.

Koenig SH. 1991. Cholesterol of myelin is the determinant of gray-white contrast in MRI of brain. Magn Reson Med. 1991;20:285-291.

Kosta P, Argyropoulou MI, Markoula S, Konitsiotis S. 2006. MRI evaluation of the basal ganglia size and iron content in patients with Parkinson's disease. J Neurol. 2006;253:26-32.

de Kruijk JR, Leffers P, Meerhoff S, Rutten J, Twijnstra A. 2002. Effectiveness of bed rest after mild traumatic brain injury: a randomised trial of no versus six days of bed rest. J Neurol Neurosurg Psychiatry. 2002;73:167-172.

Kumar A, Welti D, Ernst RR. 1975. NMR Fourier zeugmatography. J Magn Res. 1975;18:69-83.

Laurila M. 2007. MRI relaxometry of the human brain *in vivo* at 1.5 T, 3.0 T, and 4.0 T. Master of Science thesis. Tampere 2007. Tampere University of Technology. 97 p.

Lauterbur PC. 1973. Image formation by induced local interactions: examples of employing nuclear magnetic resonance. Nature. 1973;242:190-191.

Lauterbur PC. 1974. Magnetic resonance zeugmatography. Pure Appl Chem. 1974; 40:149-157.

Lees AJ, Hardy J, Revesz T. 2009. Parkinson's disease. Lancet. 2009;373:2055-2066. Review.

Lerski RA, Straughan K, Schad LR, Boyce D, Blüml S, Zuna I. 1993. MR image texture analysis--an approach to tissue characterization. Magn Reson Imaging. 1993;11:873-887.

Lichy MP, Wietek BM, Mugler JP 3rd, Horger W, Menzel MI, Anastasiadis A, Siegmann K, Niemeyer T, Königsrainer A, Kiefer B, Schick F, Claussen CD, Schlemmer HP. 2005. Magnetic resonance imaging of the body trunk using a single-slab, 3-dimensional, $T_2$-weighted turbo-spinecho sequence with high sampling efficiency (SPACE) for high spatial resolution imaging: initial clinical experiences. Invest Radiol. 2005;40:754–760.

Lichy MP, Aschoff P, Plathow C, Stemmer A, Horger W, Mueller-Horvat C, Steidle G, Horger M, Schafer J, Eschmann SM, Kiefer B, Claussen CD, Pfannenberg C, Schlemmer HP. 2007. Tumor detection by diffusion-weighted MRI and ADC-mapping--initial clinical experiences in comparison to PET-CT. Invest Radiol. 2007;42:605-613.

Ljunggren S. 1983. A simple graphical representation of Fourier-based imaging methods. J Magn Reson. 1983;54:338-343.

Lotfipour AK, Wharton S, Schwarz ST, Gontu V, Schäfer A, Peters AM, Bowtell RW, Auer DP, Gowland PA, Bajaj NP. 2011. High resolution magnetic susceptibility mapping of the substantia nigra in Parkinson's disease. J Magn Reson Imaging. 2011. doi: 10.1002/jmri.22752.

Look DC, Locker DR. 1970. Time saving in measurement of NMR and EPR relaxation times. Rev Sci Instr. 1970;41:250-251.

Lucignani G. 2007. How early? ASAP: molecular and functional imaging! Eur J Nucl Med Mol Imaging. 2007;34:596-601. Review.

Lumachi F, Tregnaghi A, Zucchetta P, Cristina Marzola M, Cecchin D, Grassetto G, Bui F. 2006. Sensitivity and positive predictive value of CT, MRI and 123I-MIBG scintigraphy in localizing pheochromocytomas: a prospective study. Nucl Med Commun. 2006;27:583-587.

MacManus MP, Seymour JF, Hicks RJ. 2007. Overview of early response assessment in lymphoma with FDG-PET. Cancer Imaging. 2007;7:10-18. Review.

Mäkelä HI, De Vita E, Gröhn OH, Kettunen MI, Kavec M, Lythgoe M, Garwood M, Ordidge R, Kauppinen RA. 2004. B0 dependence of the on-resonance longitudinal relaxation time in the rotating frame $T_1$(rho) in protein phantoms and rat brain in vivo. Magn Reson Med. 2004;51:4-8.

Mansfield P. 1977. Multi-planar image formation using NMR spin echoes. J Phys C: Solid State Phys. 1977;10:L55-58.

Markkola AT, Aronen HJ, Lukkarinen S, Ramadan UA, Tanttu JI, Sepponen RE. 2001. Multiple-slice spin lock imaging of head and neck tumors at 0.1 Tesla: exploring appropriate imaging parameters with reference to $T_2$-weighted spin-echo technique. Invest Radiol. 2001;36:531-538.

Martin WR, Wieler M, Gee M. 2008. Midbrain iron content in early Parkinson disease: a potential biomarker of disease status. Neurology. 2008;70:1411-1417.

Mazumdar M, Smith A, Schwartz LH. 2004. A statistical simulation study finds discordance between WHO criteria and RECIST guideline. J Clin Epidemiol. 2004;57:358-365.

Mazzara GP, Velthuizen RP, Pearlman JL, Greenberg HM, Wagner H. 2004. Brain tumor target volume determination for radiation treatment planning through automated MRI segmentation. Int J Radiat Oncol Biol Phys. 2004;59:300-312.

Meiboom S, Gill D. 1958. Modified spin echo method for measuring nuclear relaxation times. Rev Sci Inst. 1958;29:688-691.

Menke RA, Scholz J, Miller KL, Deoni S, Jbabdi S, Matthews PM, Zarei M. 2009. MRI characteristics of the substantia nigra in Parkinson's disease: a combined quantitative $T_1$ and DTI study. Neuroimage. 2009;47:435-441.

Michaeli S, Garwood M, Zhu XH, DelaBarre L, Andersen P, Adriany G, Merkle H, Ugurbil K, Chen W. 2002. Proton T2 relaxation study of water, N-acetylaspartate, and creatine in human brain using Hahn and Carr-Purcell spin echoes at 4T and 7T. Magn Reson Med. 2002;47:629-633.

Miller AB, Hoogstraten B, Staquet M, Winkler A. 1981. Reporting results of cancer treatment. Cancer. 1981;47:207-214.

Miller D, Barkhof F, Montalban X, Thompson A, Filippi M. 2005. Clinically isolated syndromes suggestive of multiple sclerosis, part I: natural history, pathogenesis, diagnosis, and prognosis. Lancet Neurol. 2005;4:281–288.

Mittal S, Wu Z, Neelavalli J, Haacke EM. 2009. Susceptibility-weighted imaging: technical aspects and clinical applications, part 2. Am J Neuroradiol. 2009;30:232–252.

Mischler G. 2011. Architectural Lighting Design Software web-page. [Referred Aug 11th 2011] http://www.schorsch.com/en/kbase/glossary/contrast.html

Moser E. 2010. Ultra-high-field magnetic resonance: Why and when? World J Radiol. 2010;2:37-40.

van der Naalt J, Hew JM, van Zomeren AH, Sluiter WJ, Minderhoud JM. 1999. Computed tomography and magnetic resonance imaging in mild to moderate head injury: early and late imaging related to outcome. Ann Neurol. 1999;46:70-78.

Nakada T. 2007. Clinical application of high and ultra high-field MRI. Brain Dev. 2007;29:325-335.

Neeb H, Zilles K, Shah NJ. 2006. A new method for fast quantitative mapping of absolute water content *in vivo*. Neuroimage. 2006;31:1156-1168.

Neeb H, Ermer V, Stocker T, Shah NJ. 2008. Fast quantitative mapping of absolute water content with full brain coverage. Neuroimage. 2008;42:1094-1109.

Niogi SN, Mukherjee P, Ghajar J, Johnson C, Kolster RA, Sarkar R, Lee H, Meeker M, Zimmerman RD, Manley GT, McCandliss BD. 2008. Extent of microstructural white matter injury in postconcussive syndrome correlates with impaired cognitive reaction time: a 3T diffusion tensor imaging study of mild traumatic brain injury. Am J Neuroradiol. 2008;29:967-973.

Norris DG. 2003. High field human imaging. J Magn Reson Imaging. 18;5:519-529.

Ogawa S, Menon RS, Tank DW, Kim SG, Merkle H, Ellermann JM, Ugurbil K. 1992. Functional brain mapping by blood oxygenation level-dependent contrast magnetic resonance imaging. A comparison of signal characteristics with a biophysical model. Biophys J. 1993;64:803-812.

Oouchi H, Yamada K, Sakai K, Kizu O, Kubota T, Ito H, Nishimura T. 2007. Diffusion anisotropy measurement of brain white matter is affected by voxel size: underestimation occurs in areas with crossing fibers. Am J Neuroradiol. 2007;28:1102-1106.

Pfefferbaum A, Adalsteinsson E, Rohlfing T, Sullivan EV. 2009. MRI estimates of brain iron concentration in normal aging: comparison of field-dependent (FDRI) and phase (SWI) methods. Neuroimage. 2009;47:493–500.

Pine KJ, Davies GR, Lurie DJ. 2010. Field-cycling NMR relaxometry with spatial selection. Magn Reson Med. 2010;63:1698-1702.

Pinker K, Stavrou I, Szomolanyi P, Hoeftberger R, Weber M, Stadlbauer A, Noebauer-Huhmann IM, Knosp E, Trattnig S. 2007. Improved preoperative evaluation of cerebral cavernomas by high-field, high-resolution susceptibility-weighted magnetic resonance imaging at 3 Tesla: comparison with standard (1.5 T) magnetic resonance imaging and correlation with histopathological findings--preliminary results. Invest Radiol. 2007;42:346-351.

Pohmann R, Shajan G, Balla DZ. 2011. Contrast at high field: Relaxation times, magnetization transfer and phase in the rat brain at 16.4 T. Magn Reson Med. 2011 Jun 10. doi: 10.1002/mrm.22949.

Prasad SR, Jhaveri KS, Saini S, Hahn PF, Halpern EF, Sumner JE. 2002. CT tumor measurement for therapeutic response assessment: comparison of unidimensional, bidimensional, and volumetric techniques initial observations. Radiology. 2002;225:416-419.

Purcell EM, Torrey HC, Pound RV. 1946. Resonance Absorption by Nuclear Magnetic Moments in a Solid. Phys Rev. 1946;69:37.

Rangayyan RM, Vu RH, Boag GS. 2008, Automatic delineation of the diaphragm in computed tomographic images. J Digit Imaging. 2008;21:134-147.

Rangayyan RM, Banik S, Boag GS. 2009. Landmarking and segmentation of computed tomographic images of pediatric patients with neuroblastoma. Int J Comput Assist Radiol Surg. 2009;4:245-262.

Robinson RJ, Bhuta S. 2011. Susceptibility-Weighted Imaging of the Brain: Current Utility and Potential Applications. J Neuroimaging. 2011 Jan 31. doi: 10.1111/j.1552-6569.2010.00516.x.

Rodriguez M. 1998. Computed tomography, magnetic resonance imaging and positron emission tomography in non-Hodgkin's lymphoma. Acta Radiol Suppl. 1998;417:1-36.

Rooney WD, Johnson G, Li X, Cohen ER, Kim S-G, Ugurbil K, Springer CS Jr. 2007. Magnetic field and tissue dependencies of human brain longitudinal $^1$H$_2$O relaxation *in vivo*. Magn Reson Med. 2007;57:308-318.

Römer W, Hanauske AR, Ziegler S, Thödtmann R, Weber W, Fuchs C, Enne W, Herz M, Nerl C, Garbrecht M, Schwaiger M. 1998. Positron emission tomography in non-Hodgkin's lymphoma: assessment of chemotherapy with fluorodeoxyglucose. Blood. 1998;91:4464-4471.

Rossi ME, Jason E, Marchesotti S, Dastidar P, Ollikainen J, Soimakallio S. 2010a. Diffusion tensor imaging correlates with lesion volume in cerebral hemisphere infarctions. BMC Med Imaging. 2010;10:21.

Rossi M, Dastidar P, Pertovaara H, Järvenpää R, Kellokumpu-Lehtinen P-L, Kööbi T, Heinonen T, Soimakallio S, Eskola H. 2010b. MRI vs. CT in tumour volume assessment in non-Hodgkin's lymphoma during chemotherapy. 23rd European Conference on Biomaterials ESB 2010, 11-15.9.2010, Tampere, Finland.

Rossi M, Korkola P, Pertovaara H, Järvenpää R, Dastidar P, Wu X, Eskola H, Kellokumpu-Lehtinen P-L. 2011. PET Imaging in a Longitudinal non-Hodgkin's Lymphoma Study: Association with Tumor Volume. Acta Radiol. 2011 Sep 23.

Ryvlin P, Broussolle E, Piollet H, Viallet F, Khalfallah Y, Chazot G. 1995. Magnetic resonance imaging evidence of decreased putamenal iron content in idiopathic Parkinson's disease. Arch Neurol. 1995;52:583-588.

Schenck JF, Zimmermann EA. 2004. High field magnetic resonance imaging of brain iron: A birth of a biomarker? Review article. NMR Biomed. 2004;17:433-445.

Schmidt GP, Kramer H, Reiser MF, Glaser C. 2007. Whole-body magnetic resonance imaging and positron emission tomography-computed tomography in oncology. Top Magn Reson Imaging. 2007;18:193-202.

Sale J, Lohfeld L, Brazil K. 2002. Revisiting the quantitative-qualitative debate: Implications for mixed methods. Quality & Quantity. 2002;36:43-53.

Salem KA. 2003. MRI hot topics. 3 T unlimited. Leadership in technology. Available at http://www.medical.siemens.com/siemens/de_DE/gg_mr_FBAs/files/brochures/Trio_Brochures/HotTopics_3T_Technology.pdf. Referred 25.10.2011.

Schwarz J, Weis S, Kraft E, Tatsch K, Bandmann O, Mehraein P, Vogl T, Oertel WH. 1996. Signal changes on MRI and increases in reactive microgliosis, astrogliosis, and iron in the putamen of two patients with multiple system atrophy. J Neurol Neurosurg Psychiatry. 1996;60:98-101.

Shah NJ, Zaitsev M, Steinhoff S, Zilles K. 2001. A new method for fast multislice $T_1$ mapping. Neuroimage. 2001;14:1175-1185.

Shah NJ, Neeb H, Zaitsev M, Steinhoff S, Kircheis G, Amunts K, Häussinger D, Zilles K. 2003. Quantitative $T_1$ mapping of hepatic encephalopathy using magnetic resonance imaging. Hepatology. 2003;38:1219-1226.

Shmueli K, de Zwart JA, van Gelderen P, Li TQ, Dodd SJ, Duyn JH. 2009. Magnetic susceptibility mapping of brain tissue in vivo using MRI phase data. Magn Reson Med. 2009;62:1510-1522.

Sikiö M, Holli KK, Harrison LC, Ruottinen H, Rossi M, Helminen MT, Ryymin P, Paalavuo R, Soimakallio S, Eskola HJ, Elovaara I, Dastidar P. 2011. Parkinson's Disease: Interhemispheric Textural Differences in MR Images. Acad Radiol. 2011;18:1217-1224.

Smith D, Shaffer K, Kirn D, Canellos GP, Mauch PM, Shulman LN. 1998. Mediastinal large cell lymphoma: prognostic significance of CT findings at presentation and after treatment. Oncology. 1998;55:284-288.

Sohaib SA, Turner B, Hanson JA, Farquharson M, Oliver RT, Reznek RH. 2000. CT assessment of tumour response to treatment: comparison of linear, cross-sectional and volumetric measures of tumour size. Br J Radiol. 2000;73:1178-1184.

Sormani MP, Iannucci G, Rocca MA, Mastronardo G, Cercignani M, Minicucci L, Filippi M. 2000. Reproducibility of magnetization transfer ratio histogram-derived measures of the brain in healthy volunteers. Am J Neuroradiol. 2000;21:133-136.

Steinhoff S, Zaitsev M, Zilles K, Shah NJ. 2001. Fast $T_1$-mapping with volume coverage. Magn Reson Med. 2001;46:131-140.

Specht L. 2007. 2-[18F]fluoro-2-deoxyglucose positron-emission tomography in staging, response evaluation, and treatment planning of lymphomas. Semin Radiat Oncol. 2007;17:190-197.

Symms M, Jäger HR, Schmierer K, Yousry TA. 2004. A review of structural magnetic resonance neuroimaging. J Neurol Neurosurg Psychiatry. 2004;75:1235-1244.

Tannús A, Garwood M. 1997. Adiabatic pulses. NMR Biomed. 1997;10:423-434.

Therasse P, Arbuck SG, Eisenhauer EA, Wanders J, Kaplan RS, Rubinstein L, Verweij J, Van Glabbeke M, van Oosterom AT, Christian MC, Gwyther SG. 2000. New guidelines to evaluate the response to treatment in solid tumors. European Organization for Research and Treatment of Cancer, National Cancer Institute of the United States, National Cancer Institute of Canada. J Natl Cancer Inst. 2000;92:205-216.

Therasse P, Eisenhauer EA, Verweij J. 2006. RECIST revisited: a review of validation studies on tumour assessment [Review]. Eur J Cancer. 2006;42:1031-1039.

Tran LN, Brown MS, Goldin JG, Yan X, Pais RC, McNitt-Gray MF, Gjertson D, Rogers SR, Aberle DR. 2004. Comparison of treatment response classifications between unidimensional, bidimensional, and volumetric measurements of metastatic lung lesions on chest computed tomography. Acad Radiol. 2004;11:1355-1360.

Tubridy N, McKinstry CS. 2000. Neuroradiological history: Sir Joseph Larmor and the basis of MRI physics. Neuroradiology. 2000;42:852-855.

Ugurbil K. 2005. Ultra high magnetic fields in neuroimaging. Proceedings of the high field magnetic resonance imaging and spectroscopy & magnetic resonance imaging of brain function. 2005. Minneapolis, USA. pp. 23-26.

Ungersma SE, Matter NI, Hardy JW, Venook RD, Macovski A, Conolly SM, Scott GC. 2006. Magnetic resonance imaging with T1 dispersion contrast. Magn Reson Med. 2006;55:1362-1371.

Voller B, Benke T, Benedetto K, Schnider P, Auff E, Aichner F. 1999. Neuropsychological, MRI and EEG findings after very mild traumatic brain injury. Brain Inj. 1999;13:821-827.

Vymazal J, Righini A, Brooks RA, Canesi M, Mariani C, Leonardi M, Pezzoli G. 1999. $T_1$ and $T_2$ in the brain of healthy subjects, patients with Parkinson disease, and patients with multiple system atrophy: relation to iron content. Radiology. 1999;211:489-495.

Welsch GH, Mamisch TC, Hughes T, Zilkens C, Quirbach S, Scheffler K, Kraff O, Schweitzer ME, Szomolanyi P, Trattnig S. 2008. In vivo biochemical 7.0 Tesla magnetic resonance: preliminary results of dGEMRIC, zonal $T_2$, and $T_2$* mapping of articular cartilage. Invest Radiol. 2008;43:619-626.

Welsch GH, Trattnig S, Hughes T, Quirbach S, Olk A, Blanke M, Marlovits S, Mamisch TC. 2010. $T_2$ and $T_2$* mapping in patients after matrix-associated autologous

chondrocyte transplantation: initial results on clinical use with 3.0-Tesla MRI. Eur Radiol. 2010;20:1515-1523.

Willett CG, Stracher MA, Linggood RM, Miketic LM, Leong JC, Skates SJ, Kushner DC, Jacobson JO. 1988. Three-dimensional volumetric assessment of response to treatment: stage I and II diffuse large cell lymphoma of the mediastinum. Radiother Oncol. 1988;12:193-198.

Wu X, Dastidar P, Pertovaara H, Korkola P, Järvenpää R, Rossi M, Kööbi T, Eskola H, Kellokumpu-Lehtinen PL. 2011a. Early Treatment Response Evaluation in Patients with Diffuse Large B-Cell Lymphoma-A Pilot Study Comparing Volumetric MRI and PET/CT. Mol Imaging Biol. 2011;13:785-792.

Wu X, Kellokumpu-Lehtinen PL, Pertovaara H, Korkola P, Soimakallio S, Eskola H, Dastidar P. 2011b. Diffusion-weighted MRI in early chemotherapy response evaluation of patients with diffuse large B-cell lymphoma - a pilot study: comparison with 2-deoxy-2-fluoro-D-glucose-positron emission tomography/computed tomography. NMR Biomed. 2011 Mar 8. doi: 10.1002/nbm.1689.

Youdim MB, P Riederer P. 1993. The role of iron in senescence of dopaminergic neurons in Parkinson's disease. J Neural Transm Suppl. 1993;40:57-67.

Yuan W, Holland SK, Schmithorst VJ, Walz NC, Cecil KM, Jones BV, Karunanayaka P, Michaud L, Wade SL. 2007. Diffusion tensor MR imaging reveals persistent white matter alteration after traumatic brain injury experienced during early childhood. Am J Neuroradiol. 2007;28:1919-1925.

Zaitsev M. 2002. Development of methods for functional magnetic resonance imaging and relaxation time mapping. Dissertation. Köln. Universität zu Köln. Mathematisch-Naturwissenschaftlich Fakultät. 164 p.

Zaitsev M, Steinhoff S, Shah NJ. 2003. Error reduction and parameter optimisation of the TAPIR method for fast $T_1$ mapping. Magn Reson Med. 2003;49:1121-1132.

Zhang J, Zhang Y, Wang J, Cai P, Luo C, Qian Z, Dai Y, Feng H. 2010. Characterizing iron deposition in Parkinson's disease using susceptibility-weighted imaging: an in vivo MR study. Brain Res. 2010;1330:124-130.

Zhang K, Johnson B, Pennell D, Ray W, Sebastianelli W, Slobounov S. 2010. Are functional deficits in concussed individuals consistent with white matter structural alterations: combined FMRI & DTI study. Exp Brain Res. 2010;204:57-70.